Stable Silicon Isotopes Uncover a Mineralogical Control on the Benthic Silicon Cycle in the Arctic Barents Sea (EarthArXiv PREPRINT)

This manuscript has been submitted for publication in Geochimica et Cosmochimica Acta. Please note that this manuscript is currently in peer-review and has yet to be formally accepted for publication. Subsequent versions of this manuscript may have slightly different content. If accepted, the final version of this manuscript will be available via the 'Peer-reviewed Publication DOI' link on the right-hand side of this webpage. It is understood that all persons copying this information will adhere to the terms and constraints invoked by each author's copyright. This work may not be reposted without explicit permission of the copyright owner. Please feel free to contact the corresponding author, we welcome any feedback.

Author for correspondence: James Ward, School of Earth Sciences, University of Bristol (JamesPJ.Ward@bristol.ac.uk)

EarthArXiv PREPRINT: Stable Silicon Isotopes Uncover a Mineralogical Control on the Benthic Silicon Cycle in the Arctic Barents Sea

James P. J. Ward[1,*], Katharine R. Hendry[1], Sandra Arndt[2], Johan C. Faust[3,7], Felipe S. Freitas[1], Sian F. Henley[4], Jeffrey W. Krause[5,6], Christian März[7], Hong Chin Ng[1], Rebecca A. Pickering[8]

[1]*School of Earth Sciences, University of Bristol, Bristol, BS8 1QE, UK*

[2]*BGeosys, Department of Geosciences, Université libre de Bruxelles, Brussels, CP160/03 1050, Belgium*

[3]*MARUM - Center for Marine Environmental Sciences, University of Bremen, Bremen, 28359, Germany*

[4]*School of GeoSciences, The University of Edinburgh, Edinburgh, EH9 3FE, UK*

[5]*Dauphin Island Sea Lab, Dauphin Island, AL, USA*

[6]*School of Marine and Environmental Sciences, University of South Alabama, Mobile, AL, USA*

[7]*School of Earth and Environment, University of Leeds, Leeds, LS2 9JT, UK*

[8]*Department of Geology, Lund University, Sölvegatan 12 223 62, Lund, Sweden*

Author for correspondence: JamesPJ.Ward@bristol.ac.uk[*]

Abstract

Biogeochemical cycling of silicon (Si) in the Barents Sea is under considerable pressure from physical and chemical changes, including dramatic warming and sea ice retreat, together with a decline in dissolved silicic acid (DSi) concentrations of Atlantic inflow waters since 1990. Moreover, further expansion of the Atlantic realm (termed 'Atlantification') is expected to shift phytoplankton community compositions away from diatom-dominated spring blooms in favour of Atlantic flagellate species (coccolithophore-dominated). The changes in pelagic primary production will alter the composition of the material comprising the depositional flux, which will subsequently influence the recycling processes at and within the seafloor. In this study we assess the predominant controls on the early diagenetic cycling of Si, a key nutrient in marine ecosystems, by combining stable isotopic analysis of pore water DSi and of operationally defined reactive pools of the solid phase. We show that low biogenic silica (BSi) contents (0.39-0.52 wt% or 92-185 μmol g dry wt^{-1}) drive correspondingly low asymptotic

concentrations of pore water DSi (∼100 μM). However, while these surface sediments appear almost devoid of BSi, we present evidence for the rapid recycling of bloom derived BSi that generates striking transient peaks in sediment pore water [DSi], which is a feature that is subject to future shifts in phytoplankton community compositions. Using a simple mass balance calculation we show that the pore water DSi pool is supplemented by a lithogenic Si source (LSi), while our sediment pore water Si isotopic profiles also uncover a coupling of the iron (Fe) and Si cycles. This has previously been observed in lower latitude marine sediment systems and thus provides further support for a redox influence on oceanic pore water DSi. We suggest that a high LSi:BSi ratio and apparent Fe (oxyhydr)oxide influence could lead to a degree of stability in the annual background benthic flux of DSi despite the pressures on pelagic phytoplankton communities. Coupled with supporting isotopic evidence for the precipitation of authigenic clays in Barents Sea sediment cores, our observations have implications for the sink *vs* recycling terms in the regional Si budget.

Keywords: Silicon Isotopes, Benthic Flux, Pore Water, Reactive Pools

1. Introduction

The Barents Sea represents a highly productive gateway that joins the Atlantic and Arctic Oceans. This shelf sea accounts for ∼40% of the total Arctic Ocean primary production, despite occupying just 10% of the areal extent (Smedsrud et al. (2013); Oziel et al. (2016) and references therein). However, the Barents Sea is at present subject to considerable climate-driven perturbations, including the highest rates of winter sea ice loss (47% in March from 1979-2018) (Årthun et al., 2012; Smedsrud et al., 2013; Docquier et al., 2020) and surface water warming (Lind et al., 2018) observed across the Arctic Ocean. Much of this sea ice melt and surface water warming is driven by an expansion of the southern Atlantic Water (AW) realm ('Atlantification'), which is separated from the Arctic Water mass (ArW) of the northern Barents Sea by the oceanic polar front (PF) (Årthun, 2011; Oziel et al., 2016) (Fig. 1). The consequences of these changes are predicted to have significant implications for CO_2 uptake in the surface ocean, long term carbon sequestration, deep water formation, nutrient cycling in the pelagic and benthic realms, as well as the balance of marine ecosystems and

primary production in the Barents Sea (Oziel et al., 2016; Freitas et al., 2020; Haug et al., 2017; Faust et al., 2021; Lind et al., 2018).

At present, phytoplankton spring blooms of the Arctic Ocean are a cornerstone event that make up a significant proportion of annual primary productivity across the region (Krause et al., 2018). The community composition of spring and early summer blooms is typically dominated by diatoms, a photosynthesising microalgae that uses dissolved silicic acid (DSi) to build frustules of biogenic silica (BSi), commonly termed 'opal' (Krause et al. (2019, 2018); Giesbrecht and Varela (2021); Downes et al. (2021) and references therein). Seawater is undersaturated with respect to the solubility of BSi, which facilitates dissolution as diatoms and other silicifiers die and sink through the water column down to the seafloor following a bloom (Tréguer et al., 1995; Frings, 2017). Crucially, ∼30% of this dissolution globally occurs at or just below the sediment-water interface (SWI) during early diagenesis, creating strong concentration gradients between the upper sediment pore and ocean bottom waters (Tréguer et al., 2021). This recycling process drives DSi fluxes back to the water column (Frings, 2017), which is a major component of the ocean Si nutrient cycle and thus has significant implications for the global carbon cycle by sustaining subsequent diatom blooms locally (e.g. shallow systems) or non-locally (nutrients advected or mixed into the euphotic zone) (Loucaides et al., 2012; Dixit and Van Cappellen, 2003).

In addition to the recycling of diatom-derived BSi, other sources of DSi in marine sediment pore waters include the dissolution of siliceous sponge spicules (Ng et al., 2020), radiolarian tests (Maldonado et al., 2019) and lithogenic minerals (LSi) (Geilert et al., 2020; Fabre et al., 2019; Ehlert et al., 2016b). The release of DSi from LSi phases has long been theorised in the North Atlantic to explain the magnitude of benthic recycling fluxes in sediments relatively devoid of BSi (Tréguer et al., 1995; Tréguer and De La Rocha, 2013). This dissolution is driven by North Atlantic bottom water DSi concentrations ([DSi]) (∼10-40 μM), which are well below that of many LSi mineral solubilities (Tréguer et al., 1995) (130 μM, 70 μM and 100 μM for montmorillonite, kaolinite and quartz in seawater respectively (Mackenzie et al., 1967; Lerman et al., 1975; Schink et al., 1975)). Furthermore, Ng et al.

(2020) suggested that an increase in pore water [DSi] in cores of elevated [Fe] from the Greenland shelf was driven by both DSi desorption from Fe (oxyhydr)oxides (FeSi) as they reductively dissolve and through an increase in the solubility of BSi due to the removal of protective oxide coatings. This supports the hypothesis that redox reactions can regulate pore water DSi by influencing BSi dissolution kinetics (Aller, 2014; Ng et al., 2020).

The build-up of pore water DSi from BSi, LSi and FeSi sources is curbed by uptake through the precipitation of authigenic clays (AuSi) (Ehlert et al., 2016a; Geilert et al., 2020; Loucaides et al., 2010; Michalopoulos and Aller, 1995). The precipitation of AuSi can operate either through the dissolution of LSi and subsequent coprecipitation of DSi with dissolved aluminium (Al), or through a reverse weathering pathway whereby BSi reacts with Al/Fe (oxyhydr)oxides and major cations present in pore waters (Ehlert et al. (2016a) and references therein). This forms potassium, magnesium and Fe-rich aluminosilicates described as 'green clay', or glauconite, which is a common product of BSi weathering (Ehlert et al., 2016a; Loucaides et al., 2010; Aller, 2014). These clays can act as a significant sink for silicon (Si) in the marine environment (Rahman et al. (2017); Sutton et al. (2018) and references therein).

The balance of DSi release and uptake processes in marine sediments act to modulate the magnitude of benthic fluxes of DSi from Arctic shelf sediments (0.34 Tmol yr^{-1}), which are estimated to be as important for the regional Si budget as circum-Arctic rivers (∼0.4 Tmol yr^{-1}) (März et al., 2015). Globally, rivers are estimated to contribute ∼55% of the total Si input (including dissolved and amorphous Si) to the ocean Si budget (Tréguer et al., 2021). However, a 20% decrease in [DSi] has been observed in Barents Sea Atlantic inflow waters from 1990-2012 (Rey, 2012) and recent evidence suggests a kinetic limitation on diatom growth by surface water [DSi] in blooms off Svalbard (Krause et al., 2018), as well as in the Pacific and Canadian Arctic regions (Giesbrecht and Varela, 2021; Giesbrecht, 2019). This is compatible with the suggestion that a northward expansion of the AW realm will shift phytoplankton communities in favour of Atlantic flagellate species (e.g. *Emiliania huxleyi* and *Phaeocystis*), threatening to reduce the depositional flux of BSi to Arctic sediments

(Neukermans et al., 2018; Orkney et al., 2020). It is therefore crucial to better understand how sensitive the benthic Si system is to further perturbations, given the pressures the Barents Sea and wider Arctic region face from anthropogenic warming and Atlantification. As a result, recent work has begun to develop a better mechanistic understanding of this subject through measurement of stable Si isotopes (Ehlert et al., 2016a; Geilert et al., 2020; Ng et al., 2020; Cassarino et al., 2020).

The aim of this work is to further develop our mechanistic understanding of the early diagenetic cycling of Si in Arctic marine sediments through stable Si isotopic analysis on pore water DSi and its solid phase sources. We address specific research questions, including: 'What is the magnitude of the benthic DSi flux?', 'What are the sources of pore water DSi near the SWI?', 'Is there evidence of AuSi precipitation or a redox control on the benthic Si system?' and 'What are the key geographic and temporal variations?'.

2. Materials and methods

2.1. Field methods

During the Changing Arctic Ocean Seafloor (ChAOS) sampling campaign sediment cores were collected from the Barents Sea Opening (B03) and from five stations along a 30^{o}E transect between 74 and 81^{o}N in the central Barents Sea (B13-B17) over three consecutive years (2017-2019). This sampling was carried out to assess the temporal and spatial dynamics of the benthic Si system (Fig. 1, Table 1). Samples were collected between late June and early August aboard the RRS *James Clark Ross* (JR16006, JR17007 and JR18006), with sampling targeted at sites of similar water depth (286-367 m) (Table 1). Cruise reports are available, which include all accompanying details and complementary data (Hopkins, 2018; Solan, 2018; Barnes, 2019).

Sampling for sediment and pore water analysis was carried out with a Multicorer from UK National Marine Facilities. This device allowed for sampling of the upper 30-40 cm of sediment including the overlying core top water and intact SWI. For solid phase sampling, the core tubes were placed onto a manual core extruder and slices were taken with a Perspex

Table 1: Sampling station information averaged across the three cruises.

Station	Latitude (^{o}N)	Longitude (^{o}E)	Water Depth (m)	Bottom Water Temp (^{o}C)
B03	72.6342	17.9224	367	3.9
B13	74.4331	29.9532	359	1.8
B14	76.5019	30.5012	295	1.9
B15	78.2192	29.9574	317	-1.5
B16	80.0982	30.0257	286	-1.5
B17	81.2825	29.6153	337	1.8

plate (sampling resolution of 0.5 cm intervals from 0-2 cm below seafloor (cmbsf), 1 cm from 2 cmbsf), which were then stored at -20^{o}C. For the dissolved phase, the overlying core top water was collected first, after which pore water samples were extracted with Rhizon filters attached to 30 mL plastic syringes, using spacers to create a vacuum (sampling resolution of 1 cm from 0.5-2.5 cmbsf, 2 cm to 20.5 cmbsf, 5 cm to 35.5 cmbsf). Pore waters were then acidified with Romil UpA HCl and stored at 4^{o}C.

For sediment pore water element concentration analysis, pore waters were collected from three separate Multicorer deployments at each station and year (Fig. 2). One of the replicate deployments for each year at B13, B14 and B15 were also sampled for Si isotopic analysis (Fig. 3). These three stations span the three main hydrographic domains of the Barents Sea (AW, PF and ArW) (Fig. 1).

Sediment core incubations were carried out on-board in 2019 to quantify benthic DSi fluxes. An air tight cap was sealed over the top of the core tube, which incorporated a plastic tube where a 60 mL plastic syringe could be connected for sample collection (see Fig. S3 for a schematic). A magnetic stirrer was attached to the base of the cap to gently homogenise the core top water. The incubation was run over a 24 hour period, with 50 mL samples extracted through an Acrodisc filter (0.2 μm) at 3 hour intervals.

2.2. DSi concentration analysis of pore waters and seawater

[DSi] analysis of pore water samples, as well as the incubation samples from 2019 (see section 4.1) were carried out on-board using a Lachat QuikChem 8500 flow injection auto-analyser. Internationally certified reference materials for seawater nutrients (KANSO Ltd., Japan) were used to define the accuracy associated with this method, which averaged 2.8% across the three cruises (1.5-5%).

2.3. Solid phase extraction and DSi concentration analysis

Operationally defined reactive pools of Si were extracted from the solid phase following Pickering et al. (2020). An additional study was also carried out here to assess the influence of oven drying and grinding sediment samples prior to isotopic analysis (see supp. section 2). This sequential digestion procedure separates Si into operational pools based on the conditions, kinetics (time dependent) and sequence of the reaction (Pickering et al., 2020; Rahman et al., 2016; Michalopoulos and Aller, 2004; DeMaster, 1981). Reagents were added to 50-70 mg of thawed (dry weight) or dried sediment in the following sequence: 36 mL 0.1 M HCl (in-house distilled) for 18 hours (Si-HCl pool); 25 mL 0.1 M Na_2CO_3 (Sigma-Aldrich BioXtra) for 5 hours in an 85^{o}C water bath (Si-Alk pool); 10 mL 4 M NaOH (Honeywell Fluka Trace SELECT) for 2 hours at 85^{o}C (Si-NaOH pool). Predominantly, these sequential extractions are thought to remove authigenic metal oxide coatings, BSi and LSi phases respectively (Michalopoulos and Aller, 2004; Pickering et al., 2020). In addition to the digestion sequence applied by Pickering et al. (2020), here 5 mL of 10% H_2O_2 (Fisher Chemical Extra Pure SLR) was added to the sediment samples for 30 minutes after the 0.1 M HCl leach to remove diluting organic phases (Mortlock and Froelich, 1989). After each digestion, supernatants were extracted after centrifugation and the residual sediment was rinsed in triplicate with Milli-Q water (18.2 MΩ) to remove any remaining reagent.

The use of Na_2CO_3 to remove BSi relies on the difference between rapid, nonlinear dissolution of BSi and the slower, linear dissolution of LSi (DeMaster, 1981). The traditional intercept method was employed for BSi concentration analysis, whereby aliquots of Na_2CO_3 are extracted at 2, 3 and 5 hr intervals over the course of the digestion. The [DSi] of

the aliquots were plotted as a function of time and the extrapolated intercept of a linear regression was taken as the sediment sample BSi content (DeMaster, 1981) (Fig. S4). It is known that the intercept method encapsulates some degree of contamination from LSi dissolution. For example, Barão et al. (2015) have shown that non-biogenic phases can be released into the Na_2CO_3 solution within the initial non-linear phase of the digestion (Fig. S4B). Ragueneau and Tréguer (1994) estimate that this interference represents ∼15% of the BSi content calculated from the intercept of the linear regression. In order to minimise LSi contamination for isotopic analysis of the BSi phase, digestion experiments were ceased at 20 minutes by neutralisation with in-house distilled HCl. The [DSi] in the 20 minute Na_2CO_3 extractions were all found to be below the linear regression intercept, thus contamination from LSi is thought to be minimal (Fig. S4). Corrections for LSi interference following Kamatani and Oku (2000) and Ragueneau et al. (2005) were carried out to confirm this assumption (see supp. section 3). These calculations were found to depend strongly on the inferred Si/Al ratio of the LSi phase, however the results suggest a low degree of LSi interference in the 20 minute extraction (1.5-8%) (Table S1).

After neutralising and separating the 20 minute Na_2CO_3 supernatant from the sediment sample centrifuge tubes, 25 mL of fresh Na_2CO_3 was added and the digestion resumed for a further 5 hours to allow for the complete removal of BSi prior to the NaOH digestion.

[DSi] in the leachate samples collected from the sequential digestion experiments were measured chlorometrically by molybdate blue spectrophotometry (Heteropoly Blue Method) (Strickland and Parsons, 1972) on a VWR V-1200 spectrophotometer at the University of Bristol. This method has an analytical precision of 2-3% (RSD), with a slightly higher average reproducibility of triplicate samples normalised to sediment dry weight of 5.5% (range 0.09 to 16.4%). This external reproducibility is higher as it captures environmental factors, including spatial heterogeneity.

2.4. Isotopic analysis

2.4.1. Sample preparation (DSi co-precipitation and column chemistry)

Core top and pore water samples were pre-concentrated prior to isotopic analysis by the Mg-induced co-precipitation (MAGIC) method following Karl and Tien (1992) and De Souza et al. (2012). Sample preparation was carried out in a clean setting at the University of Bristol's, Bristol Isotope Group (BIG) laboratory. This method involves the adsorption of Si to brucite ($Mg(OH)_2$) as it precipitates from seawater, which concentrates the Si and reduces the cation and anion matrix by up to two orders of magnitude, allowing for the effective use of cation exchange resin columns (De Souza et al., 2012). Brucite precipitation is induced by the addition of 1 M NaOH (Titripur) to pH-neutral samples in two steps. After both 1 M NaOH additions the samples were centrifuged and the supernatant removed. Precipitates were rinsed with 0.001 M NaOH solution to remove excess ions (Na^+, Cl^-, ${SO_4}^{2-}$, Ca^{2+}, K^+) after the second precipitation cycle (Ng et al., 2020). Samples were dissolved for column chemistry by the addition of 60-200 μL in-house distilled HCl (depending on sample size) and diluted with Milli-Q.

The pre-concentrated sea and pore water samples, filtered solid phase leachates and reference standards were all passed through cation exchange columns, following Georg et al. (2006). Here, a resin (Bio-Rad AG50W-X12) was used for the chromatographic separation of Si from sea water matrix (De Souza et al., 2012). Each sample was loaded onto the columns and eluted with the required volume of Milli-Q to produce a 2 ppm solution. This method retains ambient cations (e.g. Na^+, Mg^{2+}, Fe^{2+}) and does not attract DSi as non-ionic orthosilicic acid (H_4SiO_4) or the negatively charged species ${H_3SiO_4}^-$, which are in equilibrium at pH 2-8 (Georg et al., 2006). Samples were collected with acid-cleaned Nalgene LDPE bottles and the Si isotopic composition was analysed within 48 hours of column chemistry.

2.4.2. Mass spectrometry

Stable Si isotopic compositions were measured on a Finnigan Neptune Plus High Resolution MC-ICP-MS by Thermo Fisher Scientific in the BIG laboratory. Data acquisition was carried out through numerous sessions over two years. Si solutions were transferred from the

autosampler via a PFA Savillex C-flow nebuliser (100 μl min^{-1}) connected either to a PFA Teflon barrel spray chamber or an Apex IR Desolvating Nebulizer.

Most samples analysed for their Si isotopic composition were measured in duplicate or triplicate (80 of 123 pore and core top water samples and 39 of 45 sediment leachates) using a standard-sample bracketing technique (De La Rocha, 2002) and were blank corrected. The intensity of ^{28}Si in the 0.1 M HCl blank was <1% of the sample intensity in every analytical session. Each standard and sample was doped with Mg (10 ppm Inorganic Ventures) to further address mass bias and instrumental drift through internal standard normalisation (Cardinal et al., 2003), as well as with 0.001 M H_2SO_4 (ROMIL-UpA) and 1 M HCl to counteract anionic matrix effects ($SO_4{}^{2-}$ and Cl^-) (Hughes et al., 2011; Van Den Boorn et al., 2009).

Stable Si isotopic compositions are reported in δ^nSi notation in units of per mil (‰) (equation 1), which represents a deviation of the ^{30}Si/^{28}Si or ^{29}Si/^{28}Si ratio of the sample relative to the international standard NBS-28.

$$\delta^n Si = \left(\frac{({}^n Si/{}^{28} Si)_{sample}}{({}^n Si/{}^{28} Si)_{standard}} - 1 \right) \cdot 1000 \quad (1)$$

Data quality was assessed through the correlation between δ^{29}Si and δ^{30}Si ($R^2 = 0.997$). Isotopic data presented here falls on a mass dependent fractionation line of gradient 0.5119 (Fig. S5), which is in between that expected of mass dependent kinetic (0.5092) and equilibrium (0.518) Si isotope fractionation (Reynolds et al., 2007; Cardinal et al., 2003). Regular analysis of reference standards was carried out in each analytical session to quantify the long-term external reproducibility of sample measurements to 2 standard deviations (2σ). The mean values of standards measured in this study (Diatomite +1.24 ±0.14‰ (n=116); LMG08 -3.47 ±0.13‰ (n=46); $ALOHA_{1000}$ +1.23 ±0.17‰ (n=30)) agree well with published values (+1.26 ±0.2‰ (Reynolds et al., 2007); -3.43 ±0.15‰ (Hendry et al., 2011; Hendry and Robinson, 2012); +1.24 ±0.2‰ (Grasse et al., 2017) respectively) (Fig. S6). Measurement replicate reproducibility (2σ) ranges from 0.01 to 0.30‰ for pore waters, 0.10 to 0.19‰ for core top waters and 0.01 to 0.23‰ for sediment leachates, averaging 0.11‰.

2.5. Metal concentrations

The concentrations of a suite of metals (Al, Ti, Fe, Mn, Mg, V) were determined in the sediment extraction leachates (0.1 M HCl, 0.1 M Na_2CO_3, 4 M NaOH) by Inductively Coupled Plasma-Optical Emission Spectroscopy (ICP-OES) at the University of Bristol, using an Agilent Technologies 710 (Fig. S2). Analytical performance was assessed throughout the four sessions by periodic measurement of blanks and calibration standards. RSD (1σ) ranged from 0.25-12.75%, averaging 2.70% across repeat standard measurements (n=22) and all elements analysed.

2.6. Benthic flux calculations

The core top water [DSi] (μM) of each sample extraction from the incubation experiments was plotted as a function of the ratio of time:core top water height (day m^{-1}) (Fig. 4). The gradient of the linear regression represents the flux magnitude (mmol m^{-2} day^{-1}) and the total benthic flux (J_{tot}), as it takes into account molecular diffusion, advection, bioturbation and bioirrigation. This method corrects the rate of DSi release over time for the influence of sample removal at each time interval following Hammond et al. (2004) and Ng et al. (2020). The flux magnitude uncertainties were obtained from the error on the gradient of the linear regression (Fig. 4).

Molecular diffusive fluxes (J_{diff}) were also calculated using Fick's first law of diffusion while assuming a linear [DSi] gradient across the SWI (equation 2-4). A linear gradient assumption uses the [DSi] at ~0 cmbsf (core top water) and the uppermost sediment porewater (0.5 cmbsf). Previous studies have also employed an exponential curve fitting methodology to determine DSi flux magnitudes (Frings, 2017; Ng et al., 2020; McManus et al., 1995). Both methods were compared here (Table 2) and it was deemed that the linear assumption was more appropriate for the Barents Sea stations (please see supp. section 4 for the discussion).

$$\theta = 1 - \ln(\phi^2) \tag{2}$$

$$D_{sed} = D_{sw} \,/\, \theta \tag{3}$$

$$J_{diff} = -\phi \cdot D_{sed} \cdot (d[DSi] \,/\, dz) \tag{4}$$

, where θ represents sediment tortuosity, ϕ is porosity in the surface sediment, D_{sed} is the is the diffusion coefficient of DSi in seawater (D_{sw}) corrected for tortuosity (Boudreau, 1996) and $d[DSi]/dz$ is the [DSi] gradient across the SWI. D_{sw}, which is dependent on temperature (T) and viscosity (η), was determined based on an empirical relationship derived from an experimental study (Rebreanu et al., 2008) (equation 5), using bottom water temperatures measured at each station in 2017 (Table 1).

$$D_{sw} = 3.33 \times 10^{-12} \cdot (T \,/\, \eta) \tag{5}$$

, where D_{sw} is in $cm^2\ s^{-1}$, T in kelvin and η in poises (g $cm^{-1}\ s^{-1}$).

3. Results

3.1. Pore water

3.1.1. DSi concentration profiles

Overall, pore water asymptotic DSi concentrations of the Barents Sea are similar to those of the nearby Norwegian Sea ($\sim$100 μM) and North Atlantic Ocean (99-230 μM) (Ragueneau et al., 2001; Rickert, 2000; Sayles et al., 1996). In general [DSi] profiles analysed from the northern, ArW sites (B15, B16, B17) (Fig. 1) are more alike between both the coring events within one cruise and between the three cruise years when compared with the AW stations (B03, B13, B14) (Fig. 2). Station B15 exhibits a typical downcore exponential increase in DSi to an asymptotic value (Aller, 2014) of approximately 100 μM at 3 cmbsf (Fig. 3), while station B13 also displays a rapid increase in [DSi] in the upper pore waters to a similar concentration as B15, but continues to gradually increase with depth. Station B14 [DSi] profiles are highly variable, presenting with striking peaks in 2017 and 2019 of up to 300 μM at 2.5-3 cmbsf, also showing a gradual release of DSi towards the base of the sediment cores (Fig. 2 and 3).

3.1.2. Benthic DSi flux magnitudes

Diffusive flux (J_{diff}) magnitudes calculated using Fick's first law of diffusion (equation 4) with a two-point linear assumption of the concentration gradient at the SWI of B13, B14 and B15 across the cruise years range from +0.05 to +0.44 mmol m^{-2} day^{-1} (mean +0.21 ±0.23 mmol m^{-2} day^{-1} (2σ, n=27)). J_{tot} values derived from the 2019 on-board incubation experiments range from +0.08 ±0.06 to +0.19 ±0.13 mmol m^{-2} day^{-1} (Fig. 4, Table 2). These values are within range of a pan-Arctic review of shelf sediment DSi fluxes (J_{tot}) (-0.03 to +6.2 mmol m^{-2} day^{-1}, mean +0.6 ±1.3 mmol m^{-2} day^{-1}, where a negative flux indicates DSi diffusion from bottom waters into the sediment) (Fig. S7) (Bourgeois et al., 2017).

3.1.3. Isotopic composition of DSi

$\delta^{30}Si_{DSi-PW}$ values fall within range of those previously analysed in marine pore waters (Opfergelt and Delmelle, 2012; Sutton et al., 2018; Frings et al., 2016), ranging from -0.51 to +1.69 (±0.14‰ 2σ). Station B13 $\delta^{30}Si_{DSi-PW}$ ranges from +0.30 to +1.36‰, B14 is the most variable ranging from -0.51 to +1.69‰ and B15 from +0.53 to +1.63‰. Only two of nine cores were found to have a $\delta^{30}Si_{DSi-PW}$ composition at the base within error of that at 0.5 cmbsf (B14 and B15 2019), most tend towards isotopically lighter compositions with depth (Fig. 3). The composition of core top waters from 2017 ($\delta^{30}Si_{DSi-CT}$) are similar across the three sites (B13 +1.64 ±0.19‰ (n=5), B14 +1.46 ±0.15‰ (n=3), B15 +1.69 ±0.18‰ (n=6)). $\delta^{30}Si_{DSi-CT}$ at B13 is within long term reproducibility of the composition of North Atlantic Waters (+1.55 (De Souza et al., 2012; Varela et al., 2016)) and B15 presents with a similar composition to that of Arctic deep waters of the Beaufort shelf (+1.84 ±0.10‰ at the halocline (125-200 m)) and Canada Basin (+1.88 ±0.12‰ below 2000 m) (Varela et al., 2016).

3.2. Solid phase

3.2.1. BSi content

BSi contents were measured in the surface sediment interval (0-0.5 cmbsf) across the three sites for 2019 samples, which ranged from 0.39-0.52 wt% (92-185 μmol g dry wt^{-1}),

Table 2: Parameters used to calculate the benthic fluxes of DSi through the two-point linear and exponential curve-fitting techniques. Please see supp. section 4 for a discussion on the curve fitting methodology. All values for the diffusive fluxes (J_{diff}) represent a mean of triplicate coring events for each station and cruise year. Porosity (ϕ) was determined in the surface interval for JR16 (2017) samples, which was then used as the assumed value for the following years. Uncertainty on J_{diff} represents 2σ of the triplicate cores for each cruise year. For J_{tot} uncertainty is derived from the error on the gradient. * due to a shortage of sample volume, B15 $\delta^{30}Si_{DSi-Inc}$ values represent mixtures of the 0/6 hr and 21/24 hr extractions.

Cruise	2017			2018			2019		
Station	B13	B14	B15	B13	B14	B15	B13	B14	B15
Sampling Date	17/07	30/07	20/07	14/07	25/07	17/07	07/07	13/07	10/07
Fick's First Law									
ϕ	0.90	0.91	0.92	-	-	-	-	-	-
θ^2	1.21	1.19	1.17	-	-	-	-	-	-
D_{sw} $\times 10^2$ (m^2 yr^{-1})	1.51	1.51	1.49	-	-	-	-	-	-
D_{sed} $\times 10^2$ (m^2 yr^{-1})	1.25	1.27	1.28	-	-	-	-	-	-
Linear									
$\frac{d[DSi]}{dz}$ (mmol m^{-3} m^{-1})	8400	12000	5100	4800	3900	3100	6900	11000	4300
J_{diff} (mmol m^{-2} day^{-1})	0.26	0.37	0.16	0.15	0.12	0.10	0.21	0.33	0.14
$\pm 2\sigma$	0.17	0.13	0.20	0.14	0.08	0.12	0.24	0.19	0.05
Exponential									
C_{SWI} (μM)	6.9	15.4	4.4	7.8	6.5	9.4	8.8	13.0	6.1
C_{asymp} (μM)	92	123	98	90	102	91	101	162	103
β (m^{-1})	130	175	65	78	57	57	115	93	52
$\frac{d[DSi]}{dz}$ (mmol m^{-3} m^{-1})	9600	17000	5700	6600	5400	4700	10000	14000	5100
J_{diff} (mmol m^{-2} day^{-1})	0.30	0.54	0.18	0.20	0.17	0.15	0.31	0.44	0.16
$\pm 2\sigma$	0.17	0.09	0.20	0.21	0.11	0.13	0.35	0.23	0.06
Incubation (J_{tot})									
$\frac{d(\mu MDSi)}{d(t/h)}$	-	-	-	-	-	-	0.13	0.19	0.08
$\pm$ (mmol m^{-2} day^{-1})	-	-	-	-	-	-	0.13	0.13	0.06
$\delta^{30}Si_{DSi-Inc\ 0hr}$ (‰)	-	-	-	-	-	-	1.49	1.70	-
$\delta^{30}Si_{DSi-Inc\ 3hr}$ (‰)	-	-	-	-	-	-	1.58	1.69	1.86*
$\delta^{30}Si_{DSi-Inc\ 24hr}$ (‰)	-	-	-	-	-	-	1.71	1.89	1.88*

highest at B14 underneath the PF (Fig. 5A). However, these values appear to be highly susceptible to sample preparation technique, with sediment grinding found to artificially increase BSi content by more than one-third (see supp. section 2 for discussion). The BSi contents analysed here are low relative to the Southern Ocean (∼40%), but consistent with the North Atlantic mean (<1%) (Khalil et al., 2007) and neighbouring Kara (<1 wt%) and Norwegian (<2 wt%) Seas (Kulikov, 2004; Rickert, 2000). All three cores show a decrease in BSi content with depth to ∼0.20 wt% in the mid-core (Fig. 5A). Analyses have only been carried out on samples from 2019, but it is assumed that sediment composition does not vary considerably on an interannual scale due to the generally low sedimentation rates observed in the Barents Sea since the last glacial period (0.04-2.1 mm yr^{-1}) (Faust et al., 2020).

3.2.2. Isotopic composition of the operational pools

The composition of the 0.1 M HCl leach (Si-HCl pool) was very isotopically light, averaging -2.88 ±0.17‰ (n=20), almost identical to the mean value analysed in the same leach phase of Mississippi River plume sediments (-2.89 ±0.45‰) (Pickering et al., 2020). These values were within long term reproducibility and so indistinguishable across the stations. The 0.1 M Na_2CO_3 leach (Si-Alk) composition ($\delta^{30}Si_{Si-Alk}$) was geographically distinct, presenting with values of +1.43 ±0.14‰ (n=8) and +1.50 ±0.19‰ (n=7) at B13 and B14 respectively, but +0.82 ±0.16‰ (n=14) under ArW conditions at B15 (Fig. 5B). $\delta^{30}Si_{BSi}$ of suspended particulates collected from the Beaufort Shelf and Canada Basin are isotopically heavier than this and amongst the highest values recorded for surface pelagic diatoms (+2.03 to +3.51 ±0.10‰), thought to be driven by the incorporation of sea-ice species into the assemblages (Varela et al., 2016). However, $\delta^{30}Si_{BSi}$ tends to decrease with water depth, with a value of +1.51‰ (n=1) measured at 800 m by Varela et al. (2016) and an average of +1.29‰ (n=32) analysed at a range of water depths (260 to 4100 m) across the CAO (Liguori et al., 2020). These compositions are more consistent with $\delta^{30}Si_{Si-Alk}$ at B13 and B14.

The isotopic composition of surface sample NaOH leachates ($\delta^{30}Si_{NaOH}$), a harsh alkaline digestion thought to activate the LSi pool (Pickering et al., 2020), was found to be within

uncertainty across the three stations, averaging -0.89 ±0.16‰ (n=18) and did not vary with sample preparation techniques (supp. section 2). $\delta^{30}Si_{NaOH}$ in this study is lower than that measured by Pickering et al. (2020) in the same leachate of coastal Mississippi River plume sediments (-0.54 ±0.15‰) but is within range of the mean weathered continental crust and global average clay composition (-0.57 ±0.6‰, Bayon et al. (2018)).

4. Discussion

4.1. Quantifying the benthic flux of DSi in the Barents Sea

A recent compilation estimated that the global benthic flux of DSi (comprising both J_{diff} calculations and J_{tot} from incubation experiments) ranges from -0.03 to +24.2 mmol m^{-2} day^{-1} (Ng et al., 2020). Benthic fluxes of DSi emanating from CAO basin sediments are within the lower end of this range (+0.002 to +0.035 mmol m^{-2} day^{-1}) (März et al., 2015) and an order of magnitude lower than J_{tot} measurements from Arctic shelf sediments (-0.03 to +6.2 mmol m^{-2} day^{-1}) (Bourgeois et al., 2017), but are similar to flux magnitudes estimated for Norwegian Sea sediments (+0.06 mmol m^{-2} day^{-1} (Rickert, 2000)) and the deep Northwest and Northeast Atlantic (+0.057 and +0.16 mmol m^{-2} day^{-1} respectively) (Sayles et al., 1996; Ragueneau et al., 2001). In this study of the Barents Sea, the J_{diff} (+0.05 to +0.44 mmol m^{-2} day^{-1}) and J_{tot} (+0.08 ±0.06 to +0.19 ±0.13 mmol m^{-2} day^{-1}) approximations of the benthic DSi flux are consistent within uncertainty (Table 2) and are in the range of previously published values for pan-Arctic shelf and nearby Svalbard sediments (Bourgeois et al., 2017). Despite the importance of benthic remineralisation for water column nutrient replenishment, the spatial coverage of DSi flux magnitudes is particularly sparse in the European sector of the Arctic Ocean (Fig. S7) (Bourgeois et al., 2017), which is improved by our new estimates.

Previous studies have found no systematic relationship between DSi benthic flux magnitudes and seafloor depth, latitude or temperature, although significant differences were observed with sediment lithology (Frings, 2017; Bourgeois et al., 2017). While there are substantial spatial gaps in available observational data, 88% of the Arctic seafloor is estimated

to be dominated by clay and siliceous mud (Fig. S8) (lithological data from Dutkiewicz et al. (2015)), including the Barents Sea. These lithological groups present with similar global DSi benthic flux magnitudes (+0.36 (+0.11 to +1.29) and +0.52 (+0.08 to +4.66) mmol m^{-2} day^{-1} respectively) (Frings, 2017). Therefore, following März et al. (2015), a multiplication of the calculated flux magnitude by total Arctic shelf area could be deemed a reasonable estimate for the regional contribution of Arctic shelf sediments to the DSi budget.

Our shelf sediment fluxes are an order of magnitude greater than those observed in CAO basins, consistent with the findings of März et al. (2015). If we assume a total Arctic shelf area of 5.03×10^6 km^2 (Jakobsson et al., 2003) we can build upon previous estimates for the regional delivery of DSi from Arctic shelf sediments. With a conservative shelf flux of +0.05 mmol m^{-2} day^{-1}, the lowest Barents Sea J_{diff} among the three stations, a regional contribution of 0.10 Tmol yr^{-1} is estimated. This represents 25% of the contribution from major Arctic rivers (0.4 Tmol yr^{-1}) (Holmes et al., 2012). However, if we use the mean diffusive Barents Sea flux of +0.21 mmol m^{-2} day^{-1}, we calculate a regional value of 0.38 Tmol yr^{-1}. This is comparable to März et al. (2015) and represents 94% of the riverine DSi flux, potentially 108% if the pan-Arctic riverine flux calculated by Hawkings et al. (2017) is used (0.35 Tmol yr^{-1}), providing further support for the relative importance of the DSi flux from early diagenetic cycling in Arctic shelf sediments. Furthermore, this regional estimate errs on the side of caution, given that benthic fluxes an order of magnitude greater than those observed in this study can be found in the Canadian Archipelago and Beaufort Sea (Fig. S7) (Bourgeois et al., 2017; März et al., 2015).

4.2. What are the sources of pore water DSi near the SWI?

Isotopic analysis of incubation core top water samples ($\delta^{30}Si_{DSi-Inc}$) was carried out to determine the source material fuelling the measured fluxes (Fig. 4). Si has three stable isotopes (^{28}Si, ^{29}Si, ^{30}Si), which can undergo low temperature kinetic fractionation within the DSi pools of the water column and sediment pore water as Si is released or removed through biotic and abiotic processes. It is due to this fractionation that Si isotopes can be used as a tool to trace pathways of the Si cycle. The main process removing DSi from the

water column is uptake by diatoms for the formation of BSi, which discriminates against the heavier isotope (^{30}Si) (Varela et al., 2016), the degree to which is potentially species dependant (Sutton et al., 2013; De La Rocha et al., 1997). However, dissolution of BSi is thought to either occur without isotopic fractionation, or invoke a slight enrichment in the lighter isotope in the dissolved phase (Demarest et al., 2009; Wetzel et al., 2014). AuSi forming through kinetic precipitation reactions and sorption of Si onto Fe (oxyhydr)oxides on the other hand preferentially uptake the lighter isotope to a similar degree, leaving the residual DSi relatively heavy in composition (Opfergelt and Delmelle, 2012; Hughes et al., 2013; Delstanche et al., 2009; Zheng et al., 2016).

At stations B13 and B14 we observe an increase in $\delta^{30}\mathrm{Si}_{DSi-Inc}$ between the initial ($\delta^{30}\mathrm{Si}_{DSi-Inc\ 0hr}$ of +1.49 and +1.70 ±0.14‰ respectively) and final ($\delta^{30}\mathrm{Si}_{DSi-Inc\ 24hr}$ of +1.71 and +1.89 ±0.14‰ respectively) sample measurements, albeit just within long term reproducibility of Diatomite standard measurements (2σ ±0.14‰ (n=116)) (Fig. 4, Table 2). There is little change in $\delta^{30}\mathrm{Si}_{DSi-Inc}$ across the incubation at B15, although the two samples analysed are mixtures of 0/6 hr and 21/24 hr due to inadequate sample volume and so any variation over the time period could be suppressed (Fig. 4, Table 2). Isotopic variation over the course of the incubation should reflect the composition of the material dissolving into the pore waters and subsequently being released into the core top water. Therefore, as [DSi] increases, the composition of the core top water should tend closer to that of the dissolving phase over time. A simple mass balance calculation (equation 6) shows that the observed increases in $\delta^{30}\mathrm{Si}_{DSi-Inc}$ cannot solely be driven by the dissolution of BSi or LSi, which is supported by the composition of the solid phase reactive pools, as $\delta^{30}\mathrm{Si}_{DSi-Inc\ 24hr}$ is higher than $\delta^{30}\mathrm{Si}_{Si-Alk}$ at all stations (Table 2; Table 3). This discrepancy is most apparent at B15 where the difference between $\delta^{30}\mathrm{Si}_{Si-Alk}$ and $\delta^{30}\mathrm{Si}_{DSi-Inc}$ is >1.0 ‰.

$$\delta^{30}Si_{24hr} = \delta^{30}Si_{0hr} \cdot f_{0hr} + \delta^{30}Si_{BSi} \cdot (1 - f_{0hr}) \tag{6}$$

The observed increase in [DSi] across all incubations is not significant enough to have driven the concomitant increase in $\delta^{30}\mathrm{Si}_{DSi-Inc}$, without the presence of a BSi phase much

heavier than $\delta^{30}Si_{Alk}$ measured here. Assuming $\delta^{30}Si_{DSi-Inc\ 24hr}$ represents a mixture of $\delta^{30}Si_{DSi-Inc\ 0hr}$ and the dissolving BSi (or LSi) ($\delta^{30}Si_{BSi}$), we can use the increases in [DSi] across the incubation period to determine the theoretical composition of BSi (equation 6). We find that the dissolving phase would require a composition of +4.5, +2.7 and +1.9‰ at B13, B14 and B15 respectively. These theoretical compositions are heavier than many $\delta^{30}Si$ values previously measured in BSi (-0.75 to +3.0‰, mean +1.11‰ (Frings et al., 2016; Sutton et al., 2018; Egan et al., 2012)) and $\delta^{30}Si_{Alk}$ in this study (+0.82 to +1.50‰). Both J_{diff} and J_{tot} observed here are up to two orders of magnitude lower than those of Greenland margin incubation experiments (+0.31 to +3.1 mmol m^{-2} day^{-1}) (Ng et al., 2020), therefore the relatively slow rate of DSi release from Barents Sea sediments could allow for the expression of uptake processes (precipitation or adsorption) within the core top water composition on short timescales through the incubation, rather than solely representing the composition of the dissolving phase(s). However, the gradual increase in DSi in the core top waters over the incubation period indicates that the release rate of DSi from dissolution exceeds that of the uptake processes, while the contemporaneous increase in $\delta^{30}Si_{DSi-Inc}$ implies that the latter impose a stronger isotopic fractionation on the dissolved phase than the former.

Given the difficulties in determining the sources of the pore water DSi pool through isotopic analysis of the incubation experiment samples, an assessment into the complexity of the processes controlling the $\delta^{30}Si$ of Barents Sea pore waters ($\delta^{30}Si_{PW-DSi}$) was carried out. If $\delta^{30}Si_{PW-DSi}$ values are a consequence of a simple two endmember mixing system, whereby a fluid of core top water composition (+1.46 to +1.69‰, 4-27 μM) mixes with a pure phase derived from the dissolution of BSi (~900 μM solubility (Loucaides et al., 2012; Van Cappellen and Qiu, 1997) and +0.82 to +1.50‰ $\delta^{30}Si_{Alk}$), the data points should lie along a mixing line. The mixing line was calculated using equation 7 (Geilert et al., 2020), which assumes steady state

$$\delta^{30}Si_{mix} = \frac{(\delta^{30}Si_{DSi-CT} \cdot [DSi]_{CT} \cdot f) + (\delta^{30}Si_{BSi} \cdot [DSi]_{BSisol} \cdot (1-f))}{([DSi]_{CT} \cdot f) + ([DSi]_{BSisol} \cdot (1-f))} \quad (7)$$

where CT refers to the core top water and f represents the mixing fraction between the two phases. $\delta^{30}Si_{mix}$ was calculated across a range of f values.

The pore water isotopic data do not fall on the calculated mixing lines plotted in Fig. 6A, indicating that Si cycling within the Barents Sea seafloor is not conservative and is influenced by processes that fractionate $\delta^{30}Si_{PW-DSi}$ to higher (heavier) and lower (lighter) values. To further elucidate the specific sources and sinks that combine to produce the observed [DSi] profiles, we can examine the downcore trends in [DSi] and $\delta^{30}Si_{PW-DSi}$.

All sites studied show downcore increases in [DSi] from the core top water to peak values ranging from 94-306 μM (Fig. 2), which is much lower than the theoretical solubility of pure BSi in seawater (600-1000 μM at 0-2^{o}C, 1600-1900 μM at 25^{o}C (Rickert, 2000; Lawson et al., 1978; Hurd, 1983; Van Cappellen and Qiu, 1997; Dixit et al., 2001; Rickert et al., 2002)). Asymptotic concentrations in the Barents Sea are more characteristic of deep ocean sediments (Ragueneau et al., 2001; Dixit et al., 2001) and sediment cores containing very little BSi (<1 wt%), such as in the neighbouring Norwegian Sea (100-200 μM) (Schlüter and Sauter, 2000; Rickert, 2000). This is much lower than pore water [DSi] found in BSi rich sediments of the subarctic North Pacific or Southern Ocean, where asymptotic concentrations of 500-900 μM are common (Dixit et al., 2001; King et al., 2000; Rabouille et al., 1997; Aller, 2014).

Stations B13, B14 and B15 have surface level BSi contents of 0.39 $\pm$0.09 (2σ), 0.52 $\pm$0.02 and 0.26 $\pm$0.07 wt% respectively (or 139 $\pm$33, 185 $\pm$7, 92 $\pm$24 μmol g dry wt^{-1}), which is consistent with previous work showing that the apparent solubility of BSi decreases considerably with increasing LSi:BSi ratios (Rickert, 2000; Dixit et al., 2001). This ratio has previously been used as a predictive tool for the asymptotic DSi concentration in marine sediments (Van Cappellen and Qiu, 1997; Gallinari et al., 2002). The LSi fraction estimated here at all three sites in the 0-0.5 cmbsf interval is 96% (equation 8, Sayles et al. (2001)). This value is high, but similar to those of the Greenland and Norwegian Seas (37-98%, mean 86%) (Pirrung et al., 2008) and Kara Sea to the east (84-98%, mean 88%) (Fahl et al., 2003; Rickert, 2000). A high LSi fraction could explain why asymptotic [DSi] in the Barents Sea

458 is low and similar to the solubility of many silicate minerals, as previous experiments have
459 shown that the apparent solubility of BSi reflects the weighted, cumulative solubilities of the
460 solid Si phase assemblage (Rickert, 2000; Gallinari et al., 2002).

$$\%LSi = 100 - \%(BSi + \mathrm{CaCO_3} + TOC) \tag{8}$$

461 Relative to the respective core top waters, stations B13, B14 and B15 have isotopically
462 lighter upper pore waters and higher [DSi], indicating an isotopically lighter phase is being
463 released into the DSi pool (Fig. 3). Through a simple mass balance, akin to equation 6, we
464 calculate the theoretical isotopic composition of the 0.5 cmbsf pore water interval, with the
465 assumption that the increase in [DSi] between the core top water and this depth is driven
466 solely by the dissolution of either the BSi or LSi phase (of $\delta^{30}\mathrm{Si}_{Alk}$ and $\delta^{30}\mathrm{Si}_{NaOH}$ composition
467 respectively). Below 0.5 cmbsf, the predicted $\delta^{30}\mathrm{Si}_{DSi-PW}$ is much lower than that analysed,
468 likely reflecting the precipitation of AuSi as the pore water [DSi] surpasses the solubility
469 concentration of the AuSi (see section 4.3.1). In summary, while the composition of the 0.5
470 cmbsf pore water intervals at B15 across the three cruises can be reproduced by the discrete
471 dissolution of the BSi phase, at B13 and B14 neither phase is able to reproduce the analysed
472 composition alone (Table 3). This finding points to the contemporaneous release of BSi and
473 LSi to the pore water DSi pool, which has implications for the Barents Sea Si budget, as
474 BSi dissolution represents a recycling of oceanic Si, while LSi constitutes a source of new Si
475 discharging from the seafloor.

476 The importance of LSi as a DSi source for the pore water pool was inferred in a simi-
477 lar study of Guaymas basin sediment cores (Geilert et al., 2020), as well as for diagenetic
478 products in Mississipi River plume sediment (Pickering et al., 2020). Furthermore, Tréguer
479 et al. (1995) posited that LSi could be significant for Atlantic sediments, given that [DSi] in
480 bottom waters is well below the solubility of many terrigenous minerals. This is consistent
481 with the hypothesis that non-siliceous oceanic sediments (i.e. clays and calcareous sediment)
482 contribute an estimated 64% of the global benthic Si flux (Frings, 2017) and with numerous
483 experiments that demonstrate the release of Si from silicate minerals within days of being

Table 3: Mean values of the parameters used in the upper pore water mass balance calculations (equation 6) for the three cruise years. $\delta^{30}Si_{DSi-PW}$ at 0.5 cmbsf was predicted based on two calculations simulating the sole dissolution of BSi and LSi respectively. For B15, calculations were only carried out for 2018 and 2019 as the 0.5 cmbsf $\delta^{30}Si_{DSi-PW}$ value was not available. $\delta^{30}Si_{DSi-CT}$ could only be determined for 2017 due to a lack of sufficient sample volume in subsequent years.

Parameter	B13	B14	B15
$[DSi]_{CT}$ (μM)	8.0	9.2	7.7
$\delta^{30}Si_{DSi-CT}$ (‰)	1.64	1.46	1.69
$[DSi]_{0.5cmbsf}$ (μM)	49.6	60.6	22.8
f_{CT}	0.18	0.16	0.34
$\delta^{30}Si_{Alk}$ (‰)	1.43	1.50	0.82
$\delta^{30}Si_{NaOH}$ (‰)	-0.89	-0.89	-0.89
$\delta^{30}Si_{DSi-PW}$ predicted (BSi release) (‰)	1.47	1.49	1.12
$\delta^{30}Si_{DSi-PW}$ predicted (LSi release) (‰)	-0.43	-0.52	0.0
$\delta^{30}Si_{DSi-PW}$ 0.5 cmbsf measured (‰)	1.15	1.17	1.15

placed in low [DSi] seawater at ArW temperatures (Mackenzie and Garrels (1965); Mackenzie et al. (1967); Siever (1968); Fanning and Schink (1969); Lerman et al. (1975); Tréguer et al. (2021) and references therein). Additionally, LSi dissolution has been shown to represent a significant yet previously overlooked source of DSi to beach and ocean margin sediments, which has implications for the ratio of global DSi input and recycling terms (Jeandel et al., 2011; Fabre et al., 2019; Ehlert et al., 2016b).

Digestion experiments carried out in this study show that the Si-NaOH pool, associated with soluble LSi and residual, less reactive BSi (e.g. sponge spicules and radiolarians) (Pickering et al., 2020) is isotopically light and indistinguishable in composition across the three stations ($\delta^{30}Si_{NaOH}$ of -0.89 $\pm$0.16‰). Thus, dissolution of the Si-NaOH pool could account for the shift towards lower $\delta^{30}Si_{PW-DSi}$ observed across the SWI at the three stations.

While the harsh alkaline extraction is able to activate recalcitrant BSi, the $\delta^{30}Si_{NaOH}$ measured in this study is thought to be primarily representative of the Si isotopic composition of the soluble LSi phase. This is supported by the molar Al/Si ratios (0.57-0.67) analysed in the NaOH leachates of B13, B14 and B15 (Fig. S2). These values are higher than the Al/Si of the continental crust (0.22-0.29 (Rahn (1976) and references therein)), but is within range of common clay minerals (0.48-0.96 (Kim et al. (2004); Koning et al. (2002); Rahn (1976) and references therein). Indeed, the fine-grained sediments of the ChAOS sampling stations north of B13 are dominated by the clay and silt size fraction (Faust et al., 2020). Furthermore, an Al/Si of 0.68 is much higher than that measured in BSi (diatom, sponge and radiolarian-derived) in sediment traps, marine sediments and laboratory studies, which ranges from 2.1×10^{-5} to 0.165 (0.029 mean) (Middag et al. (2009); van Bennekom et al. (1989); Hendry and Andersen (2013); Ren et al. (2013) and references therein). These values are however consistent with the average Al/Si measured in the Na_2CO_3 leachates (0.024) (Fig. S2), indicating that $\delta^{30}Si_{Alk}$ reflects the true composition of the BSi pool.

The regionally distinct $\delta^{30}Si_{Alk}$ values could represent contrasts in the community composition of the spring blooms. A range of diatom species have been identified across the three hydrographic domains in different stages of bloom development across the Barents

Sea (e.g. *Chaetoceros/Thalassiosira* at the PF/marginal ice zone (MIZ) and *Fragilariopsis/Chaetoceros/Melosira arctica* in the ArW region) (Oziel et al., 2017; Wassmann et al., 1999, 2006a) and diatom DSi uptake fractionation factors ($^{30}\epsilon$) have been found to be species dependent, ranging from -0.42 to -2.21‰ (Sutton et al., 2013; De La Rocha et al., 1997). However, this discrepancy can also be explained by contrasting bloom developmental stages from which the BSi was released. By simulating the production of BSi by diatoms, following De La Rocha et al. (1997), we show that the composition of the accumulating BSi phase is +0.82‰, when assuming an initial surface water δ^{30}Si of +2.00‰ (Varela et al., 2016) and a fractionation factor of -1.18‰ or lower (Fig. 6B).

To summarise, the benthic Si cycle of the Barents Sea cannot be characterised as a conservative system comprised of mixing between two endmember solutions, one of core top water composition and the other derived from the dissolution of BSi. We conclude there is strong evidence for the dissolution of both BSi and LSi, as well as the uptake of DSi by processes within the sediment cores. We also observe evidence for uptake processes active within the incubation experiments, potentially demonstrating that the uptake of DSi can occur on both shorter (daily) and longer (thousands of years) timescales.

4.3. Is there evidence of AuSi precipitation or a redox control on the benthic Si system?

4.3.1. Evidence of AuSi precipitation

The composition and trends of $\delta^{30}Si_{DSi-PW}$ values in the upper 3 cmbsf are similar at B14 and B15 and across the three cruises (Fig. 3), characterised by an enrichment in the heavier isotope below 0.5 cmbsf, which drives the $\delta^{30}Si_{DSi-PW}$ back towards the core top water compositions. This shift is likely to be caused by the precipitation of AuSi in Barents Sea sediments, which preferentially removes the lighter isotope. At B13 we see a deviation towards a heavier composition at the same depth interval (Fig. 3) that is consistent with AuSi formation, although the shift is within analytical uncertainty. Similar shifts have been observed in $\delta^{30}Si_{DSi-PW}$ profiles of previous studies of both temperate and high latitude systems (Geilert et al., 2020; Ehlert et al., 2016a; Ng et al., 2020).

This increase in the $\delta^{30}Si_{DSi-PW}$ is unlikely to be caused by the dissolution of a solid

phase, as the $\delta^{30}Si_{DSi-PW}$ at 3.5 cmbsf at the three stations increases to higher values than that measured in the operational pools, especially at B15 (Fig. 5B). Additionally, dissolution would not resolve the relative shift from 0.5 cmbsf to 3.5 cmbsf observed at B14 and B15 (Fig. 3), which requires enrichment in the heavier isotope downcore.

Previous assumptions as to the solubility of AuSi minerals (220-330 μM) would preclude precipitation of AuSi in Barents Sea and many North Atlantic sediments, as [DSi] remains undersaturated with respect to these minerals (Loucaides et al., 2010; Dixit et al., 2001; Ehlert et al., 2016a; Krissansen-Totton and Catling, 2020; Cassarino et al., 2020). However, dissolution experiments carried out over 8.5 years suggest that glauconite, an aluminosilicate and common weathering product of BSi (Odin and Fröhlich, 1988), has a solubility of $\sim$50 μM in seawater (Lerman et al., 1975). In addition, Wollast (1974) calculated that sepiolite, an authigenic clay mineral found to form on BSi surfaces in deep ocean sediments (Hurd, 1973), could theoretically precipitate from seawater with a [DSi] as low as 30 μM. Subsurface formation of such minerals could explain why we see an initial decrease in $\delta^{30}Si_{DSi-PW}$ as LSi dissolves, then an increase to the 3.5 cmbsf $\delta^{30}Si_{DSi-PW}$ maxima, as DSi increases past the solubility of the precipitating phase. This hypothesis is consistent with previous work evidencing the precipitation of AuSi in LSi dominated high latitude sediments (März et al., 2015).

Coupling the evidence for benthic LSi dissolution near the SWI with that for AuSi precipitation has implications for the Si budget of the global ocean. If LSi sourced from a terrestrial environment are dissolving in seafloor sediments, they represent a source for ocean DSi. If this LSi-sourced DSi is subsequently reprecipitated as authigenic clay minerals (AuSi), the AuSi term represents a true sink. This is in contrast to AuSi precipitation through BSi-sourced DSi, which represents an early diagenetic solid phase conversion (DeMaster, 2019) and thus a recycling term to the global Si budget that enhances the preservation of BSi (Frings et al., 2016). This observation could therefore alter the sink and recycling terms in sediments relatively devoid of BSi (<1 wt%), which occupy approximately one-third of the global seafloor (Tréguer and De La Rocha, 2013).

568 *4.3.2. Evidence for a redox influence on the benthic Si cycle*

569 Below 3.5 cmbsf at B13 and B14 and below 10.5 cmbsf at B15, we see an enrichment in
570 the lighter isotope downcore across all cruise years (Fig. 3) in addition to a general trend
571 towards increased [DSi] towards the base of the cores at B13 and B14 (Fig. 2), albeit at
572 a much slower rate than beneath the SWI. These observations point to the release of an
573 isotopically light Si source. The downcore increase in [DSi] is unlikely to be driven by the
574 dissolution of BSi, given that corresponding BSi contents have reached or are approaching
575 their minima of ∼0.2 wt% by the mid-core (∼15 cmbsf) (Fig. 5A). Furthermore, we have
576 presented evidence supporting the dissolution of LSi in the upper reaches of the sediment,
577 below the SWI. However, below this depth the rate of LSi dissolution is likely to slow, given
578 that pore water [DSi] at all Barents Sea stations approaches ∼100-150 μM within the upper
579 5 cmbsf, which is similar to or above the apparent Si solubility of many silicate minerals
580 (Mackenzie et al., 1967; Lerman et al., 1975) and low BSi bulk sediment in seawater at low
581 temperatures (Jones et al., 2012; Fanning and Schink, 1969; Willey, 1978).

582 Potential sources for this isotopically light pool of Si at depth are: i) the desorption of Si
583 adsorbed onto metal (oxyhydr)oxides, or ii) sponge derived BSi dissolution. The affinity of
584 Si, and particularly the lighter isotope, for Fe (oxyhydr)oxides is well documented, with $^{30}\epsilon$
585 of -1.1 to -3.2‰ enriching the residual dissolved phase in the heavier isotope (Zheng et al.,
586 2016; Delstanche et al., 2009). Following Pickering et al. (2020) we are able to demonstrate
587 the presence of such a reactive pool in all three sediment cores. The δ^{30}Si of the Si-HCl pool
588 ($\delta^{30}Si_{HCl}$), which is thought to remove Fe (oxyhydr)oxide coatings from BSi (Pickering et al.,
589 2020), averaged -2.88 ±0.17‰ and was indistinguishable within long term reproducibility
590 across the three sites. $\delta^{30}Si_{HCl}$ did however appear susceptible to contrasting sample prepa-
591 ration techniques, presenting with much higher $\delta^{30}Si_{HCl}$ values in ground sediment samples
592 (-2.56 ±0.14‰), likely as a result of LSi contamination (see supp. Section 2 for discussion).
593 The ubiquitous presence and desorption of Si from this Fe phase at the three stations could
594 explain the ^{28}Si enrichment we observe across the oxic-anoxic boundaries, as well as the
595 gradual increase in [DSi] observed below ∼3.5 cmbsf most clearly at B13.

Examination of the [Fe] pore water profiles of the same sampling stations indicates that the light isotope enrichment occurs at a similar depth interval to where Fe appears in the pore water phase (Fig. 3). This is consistent with a change in redox state to anoxic conditions, which drives the reductive dissolution of solid Fe (oxyhdr)oxides, supported by a decrease in pore water NO_3^- and O_2 concentrations (Freitas et al., 2020) (Fig. 3) at the same depth intervals. Furthermore, reaction-transport model output derived from baseline steady-state simulations of B13 and B15 (Freitas et al., 2020) indicate that the release of Fe into the dissolved phase across the redox boundaries is driven by a combination of organic matter degradation and the reoxidation of reduced species (H_2S) diffusing upwards towards the SWI (Fig. S9). The disparity in $\delta^{30}Si_{DSi-PW}$ profiles between 3.5 and 10.5 cmbsf at B13 and B15 (which reaches a peak at 8.5 cmbsf with B15 an average of +0.96‰ higher), are consistent with the different depths of the redox boundaries found at the two sites, which is shallower at B13 than at B15 (Fig. 3).

It has previously been suggested for sediments of the Greenland Shelf that the reductive dissolution of protective solid phase Fe coatings on BSi increased pore water DSi, by enhancing the reactivity of the BSi, although there appeared to be no influence on $\delta^{30}Si_{DSi-PW}$ (Ng et al., 2020). Higher $\delta^{30}Si_{DSi-PW}$ values at one station in the Peruvian Upwelling Zone were interpreted to be due to the adsorption of Si onto reactive Fe (Ehlert et al., 2016a) and a heavy $\delta^{30}Si_{DSi-PW}$ in pore fluids of elevated [Fe] (190 μM) in the Guaymas Basin was interpreted to be driven by the precipitation of Fe-Si silicates (Geilert et al., 2020). Our finding supports this previous work by identifying a redox-driven shift in $\delta^{30}Si_{DSi-PW}$ in marine sediment cores. It is likely that the low asymptotic [DSi] in the sediments studied here allows for the detection of this process, which is masked by a much larger DSi pool in other shelf seas.

Dissolution of sponge spicule derived BSi, which has been observed in core incubation experiments of Greenland shelf sediments (Ng et al., 2020), is another potential DSi source enriched in the lighter isotope ($\delta^{30}Si_{sponge}$ values range from -5.72 to +0.87‰, mean -2.1‰ (Sutton et al. (2018) and references therein)). While the release of DSi from sponge BSi

cannot be ruled out for the Barents Sea stations, the corresponding depths of negative shifts in $\delta^{30}Si_{DSi-PW}$ profiles with increasing (decreasing) pore water [Fe] ($[NO_3^-]$) indicate a redox driven coupling between Fe and Si. In addition, the $\delta^{30}Si_{HCl}$ values at all three stations provide strong evidence for the presence of an isotopically light FeSi phase in the sediment, as this digestion is highly unlikely to dissolve sponge spicules and instead thought to predominantly remove authigenic Fe (oxyhydr)oxide coatings from BSi (Pickering et al., 2020). As a result, desorption of Si from the FeSi phase is thought to be the most likely cause of the observed downcore shift towards lighter compositions at the three Barents Sea stations (Fig. 3). Coupled with the observations supporting the release of LSi in the surface sediment layers, this evidence suggests that there is a ^{28}Si enriched, mineralogical control on the DSi released into Barents Sea cores below the SWI.

4.4. What are the key geographic and temporal variations?

[DSi] profiles of the ArW stations (B15, B16, B17) (Fig. 1) show striking similarities both spatially (within sediment core replicates of one cruise) and temporally (between cruises) (Fig. 2). This is not the case for the cores of the AW dominated region (B03, B13, B14), which is most evident at B14 where there is evidence for non-steady state, transient dynamics. Here, we see strong peaks in [DSi] and consequently the benthic flux magnitudes in 2017 and 2019, which is in contrast to 2018, where the [DSi] profile presents with a more typical, asymptotic form (Fig. 3, Table 2).

Oceanic frontal zones are highly dynamic and the PF (B14, Fig. 1) of the Barents Sea is no exception, where the interleaving of multiple water masses enhances physical mixing (Barton et al. (2018) and references therein). Wassmann and Olli (2004) attributed this feature to the observed increase in particulate organic carbon (POC) export efficiency at depth underneath the Barents Sea PF, relative to stations on the adjacent sides.

In addition to the physical mixing, studying of sea ice conditions from the respective cruise years indicates that the MIZ was influencing B14 much later in 2017 and 2019 than prior to the 2018 cruise (Fig. 7). In 2018 the MIZ in the Barents Sea retreated more rapidly and earlier in the season, receding north of the polar front almost three months prior to sampling,

unlike in 2017 and 2019 when the retreat was just six weeks prior to sediment coring. The most distinct phytoplankton blooms observed in the Barents Sea are found beneath the MIZ, supported by stratification of the nutrient rich photic zone in late spring and summer as sea ice melts (Wassmann et al., 2006b; Reigstad et al., 2002; Olli et al., 2002). Phytoplankton community compositions of Barents Sea MIZ blooms are initially dominated by diatoms (Olli et al., 2002) and observations from the Fram Strait indicate that BSi export fluxes increase with sea ice cover (Lalande et al., 2013). We therefore suggest that the sediment pore water [DSi] peaks at station B14 are transient features, sourced from the dissolution of fresher, more reactive BSi relative to the background material, which is deposited under MIZ bloom conditions and results in stronger [DSi] gradients across the SWI. The resulting enhanced rate of molecular diffusion would then begin to dissipate the peak, which was complete by the time sampling was carried out in 2018.

We estimate that the bloom derived fresh BSi contributes an additional 0.23 mmol m^{-2} d^{-1} to the B14 background (2018) DSi flux of 0.12 mmol m^{-2} d^{-1} (43.8 mmol m^{-2} yr^{-1}) (Table 2), representing an increase of 192%. If we assume this elevated flux endures across the three months required to dissipate the DSi peak, which is likely an overestimation, this would equate to an additional 20.9 mmol m^{-2} to the total annual DSi flux at B14 of 64.7 mmol m^{-2} (background plus the contribution from the bloom material).

The hypothesis that fresh, bloom derived BSi is driving the [DSi] peaks observed at B14 is supported by our isotopic data. At the depth intervals corresponding to the B14 [DSi] peaks (1.5 and 2.5 cmbsf), $\delta^{30}Si_{DSi-PW}$ in 2017 (+1.61 and +1.23 ±0.14‰) and 2019 (+1.50 and +1.48 ±0.14‰), is within analytical uncertainty of $\delta^{30}Si_{Si-Alk}$ for the B14 2019 surface sediment (+1.50 ±0.19‰). However, while this isotopic similarity lends support to the dissolution of bloom derived BSi at B14, the hypothesis that both LSi dissolution and AuSi precipitation are active within the upper sediment would suggest that $\delta^{30}Si_{DSi-PW}$ and $\delta^{30}Si_{Si-Alk}$ may not be directly comparable. Preceeding studies have employed reaction-transport modelling to disentangle these processes (e.g. Cassarino et al. (2020); Ehlert et al. (2016a); Geilert et al. (2020)), which is the subject of ongoing work in this study.

Previously it was thought that dissolution rates of BSi were very slow relative to the residence time of BSi in upper seafloor sediments, leading to the assumption that the benthos represented a stable repository, unaffected by seasonal variability in surface processes and POC export (Ragueneau et al., 2001). This stability was interpreted to be due to the fact that the residence time of BSi in surface sediments (decades to centuries) is much longer than that of seasonal and interannual variation in fluxes to the seafloor (Schlüter and Sauter, 2000; Sayles et al., 1996), which is in agreement with similar findings regarding the early diagenetic remineralisation of organic matter (Sayles et al., 1994; Martin and Bender, 1988). In direct contrast to these findings, research into the Si cycle of the Porcupine Abyssal Plain (PAP) uncovered strong evidence for non-steady state, transient responses in the pore water DSi stock driven by deposition of fresh BSi phytodetritus on a seasonal timescale (Ragueneau et al., 2001). Ragueneau et al. (2001) noted an increase in the pore water DSi inventory of 19% in the upper 10 cmbsf from early spring to summer, resulting in an increase in DSi efflux of 54% across the same time interval. These increases are coeval with a significant increase in the deposition flux of BSi at the seafloor.

As with organic matter (Sayles et al., 1994), in order for variations in BSi deposition fluxes to influence pore water DSi on a seasonal time frame, the mean lifetime of the deposited material must be less than one seasonal period (1 year) (Burdige, 2006). Therefore, BSi undergoing dissolution must *a priori* have a reactivity constant (k_{diss}) of >1 yr^{-1}, as the lifetime of material undergoing first-order dissolution is equivalent to $1/k_{diss}$ (Burdige, 2006). k_{diss} of fresh diatoms in the surface ocean range from 3 to 70 yr^{-1} (Ragueneau et al., 2000). Typically, k_{diss} values of this magnitude are not found in sediment cores, however a k_{diss} of 1.38 yr^{-1} (mean lifetime of 9 months) was measured as deep as 19 cmbsf at 4850 m depth at the PAP, attributed to bioturbation by megafauna (Ragueneau et al., 2001). A bloom derived BSi k_{diss} of 1.38 yr^{-1} corresponds to a half life of six months, implying that just 25% of the material would be preserved past one year. It is therefore plausible that the periodic deposition of fresh phytodetritus associated with the Arctic spring bloom in the much shallower Barents Sea ($\sim$300 m) could readily influence sediment pore water chemistry,

especially given the effect of frontal mixing on export efficiency observed in proximity to station B14 (Wassmann and Olli, 2004).

4.5. Conclusions

This work highlights the highly dynamic nature of the Arctic benthic Si system, which involves the cycling of Si from BSi, LSi and FeSi to the DSi phase, some of which is then taken up to form AuSi. These findings provide important implications for the Arctic Ocean Si budget, as the conversion of terrestrially-derived LSi to AuSi represents a true sink term, as opposed to a recycling term, which is the case when AuSi precipitation reflects a solid phase conversion from BSi.

We show that fresh BSi derived from pelagic phytoplankton blooms is rapidly recycled in the upper reaches of the Barents Sea seafloor. This recycling process presents as distinctive, transient increases in pore water [DSi] immediately beneath the SWI, consistent with lower latitude systems (e.g. PAP, Ragueneau et al. (2001)). These [DSi] peaks appear to dissipate within six weeks to three months, as evidenced by the contrasting sea ice conditions relative to the sampling time across the three cruises.

This strong benthic-pelagic coupling for Si in the spring bloom period will probably be subject to change as the community composition of phytoplankton blooms tend towards that of the Atlantic system and the MIZ retreats northwards. This is amplified by the observed reduction in [DSi] across the subpolar North Atlantic Ocean (Hátún et al., 2017) and consequently in Barents Sea Atlantic inflow waters over the last three decades (Rey, 2012). These pressures will likely result in less favourable conditions for diatom growth, potentially exacerbating the Si-limitation observed in diatom blooms off Svalbard (Krause et al., 2018), which has also been detected across the Arctic Ocean and in the North Atlantic subpolar region (Giesbrecht and Varela, 2021; Giesbrecht, 2019; Krause et al., 2019).

These changes would significantly influence the transient dynamics observed in this study. At present, the magnitude of the benthic DSi fluxes driven by seasonal dynamics in primary productivity (2017 and 2019) at B14 represent an estimated 192% increase relative to the apparent background flux magnitude (2018). The anticipated adjustment in the composition

of pelagic primary producers that will be deposited at the SWI may hinder this recycling process in the future, thereby reducing the estimated contribution of the bloom derived material to the annual DSi benthic flux. However, here we have inferred a significant influence from mineral-derived Si (LSi and FeSi) on the background Barents Sea benthic Si system, which is almost devoid of BSi. This mineralogical control may afford an element of stability to the magnitude of the annual benthic flux of DSi. Whether this benthic-derived DSi directly influences pelagic primary production in the Barents Sea photic zone or is transported off-shelf is unclear and is the subject of ongoing research.

Acknowledgements

This research is part of the Changing Arctic Ocean Seafloor project (ChAOS) of the Changing Arctic Ocean Programme (CAO), funded by the Natural Environment Research Council (NERC) (grant no. NE/P005942/1, 2017-2022). Authors are grateful to all those involved in cruises JR16006, JR17007, JR18006 aboard the *RRS James Clark Ross*, as well as National Marine Facilities and the British Antarctic Survey for their logistical support. We also thank colleagues at the University of Bristol for technical support (Dr C. Coath, Dr L. Cassarino, Dr J. Hatton, Dr S. Bates, Ms R. Ward and Dr A. McAleer), as well as the reviewers and associate editor for their constructive comments to improve this manuscript.

Appendix A: Supplementary Material

Supplementary material has been prepared in support of this manuscript. This material includes a document comprising a detailed discussion on a series of sensitivity experiments carried out to determine the influence of solid phase sample preparation techniques on the isotopic composition of reactive pool leachates. We also present an explanation of the LSi correction calculations for the Si-Alk pool, as well as a description of the exponential curve-fitting methodology used to determine the magnitude of benthic DSi fluxes, complimentary to the linear (two-point) and incubation techniques.

Research Data

Research data associated with this article are available in the UK Polar Data Centre (UK PDC), British Antarctic Survey and can be accessed with https://doi.org/10.5285/8933AF23-E051-4166-B63E-2155330A21D8.

References

Aller, R. C. (2014). 8.11 - Sedimentary Diagenesis, Depositional Environments, and Benthic Fluxes. *Treatise on Geochemistry (Second Edition)*, 8:293–334.

Årthun, M. (2011). *Water mass transformations and air-sea exchange in the Barents Sea*. PhD thesis, University of Bergen.

Årthun, M., Eldevik, T., Smedsrud, L. H., Skagseth, and Ingvaldsen, R. B. (2012). Quantifying the influence of atlantic heat on barents sea ice variability and retreat. *J. Clim.*, 25(13):4736–4743.

Barão, L., Vandevenne, F., Clymans, W., Frings, P., Ragueneau, O., Meire, P., Conley, D. J., and Struyf, E. (2015). Alkaline-extractable silicon from land to ocean: A challenge for biogenic silicon determination. *Limnol. Oceanogr.: Methods*, 13(7):329–344.

Barnes, D. (2019). Changing Arctic Ocean Seafloor JR18006 Cruise Report, RRS James Clark Ross. Technical report.

Barton, B. I., Lenn, Y. D., and Lique, C. (2018). Observed atlantification of the Barents Sea causes the Polar Front to limit the expansion of winter sea ice. *J. Phys. Oceanogr.*, 48(8):1849–1866.

Bayon, G., Delvigne, C., Ponzevera, E., Borges, A. V., Darchambeau, F., De Deckker, P., Lambert, T., Monin, L., Toucanne, S., and André, L. (2018). The silicon isotopic composition of fine-grained river sediments and its relation to climate and lithology. *Geochim. Cosmochim. Acta*, 229:147–161.

785 Boudreau, B. P. (1996). The diffusive tortuosity of fine-grained unlithified sediments.
786 *Geochim. Cosmochim. Acta*, 60(16):3139–3142.

787 Bourgeois, S., Archambault, P., and Witte, U. (2017). Organic matter remineralization in
788 marine sediments: A Pan-Arctic synthesis. *Global Biogeochem. Cycles*, 31(1):190–213.

789 Burdige, D. (2006). *Geochemistry of Marine Sediments*. Princeton University Press.

790 Cardinal, D., Alleman, L. Y., De Jong, J., Ziegler, K., and André, L. (2003). Isotopic
791 composition of silicon measured by multicollector plasma source mass spectrometry in dry
792 plasma mode. *J. Anal. At. Spectrom.*, 18:213–218.

793 Cassarino, L., Hendry, K. R., Henley, S. F., MacDonald, E., Arndt, S., Freitas, F. S., Pike,
794 J., and Firing, Y. L. (2020). Sedimentary Nutrient Supply in Productive Hot Spots off
795 the West Antarctic Peninsula Revealed by Silicon Isotopes. *Global Biogeochem. Cycles*,
796 34(12).

797 De La Rocha, C. L. (2002). Measurement of silicon stable isotope natural abundances via
798 multicollector inductively coupled plasma mass spectrometry (MC-ICP-MS). *Geochem.*
799 *Geophys. Geosystems.*, 3(8):1–8.

800 De La Rocha, C. L., Brzezinski, M. A., and DeNiro, M. J. (1997). Fractionation of silicon
801 isotopes by marine diatoms during biogenic silica formation. *Geochim. Cosmochim. Acta*,
802 61(23):5051–5056.

803 De Souza, G. F., Reynolds, B. C., Rickli, J., Frank, M., Saito, M. A., Gerringa, L. J., and
804 Bourdon, B. (2012). Southern Ocean control of silicon stable isotope distribution in the
805 deep Atlantic Ocean. *Global Biogeochem. Cycles*, 26(2):GB2035.

806 Delstanche, S., Opfergelt, S., Cardinal, D., Elsass, F., André, L., and Delvaux, B. (2009).
807 Silicon isotopic fractionation during adsorption of aqueous monosilicic acid onto iron oxide.
808 *Geochim. Cosmochim. Acta*, 73:923–924.

809 Demarest, M. S., Brzezinski, M. A., and Beucher, C. P. (2009). Fractionation of silicon
810 isotopes during biogenic silica dissolution. *Geochim. Cosmochim. Acta*, 73:5572–5583.

811 DeMaster, D. (1981). The supply and accumulation of silica in the marine environment.
812 *Geochim. Cosmochim. Acta*, 45(10):1715–1732.

813 DeMaster, D. J. (2019). The global marine silica budget: Sources and sinks. In *Encyclopedia*
814 *of Ocean Sciences*.

815 Dixit, S. and Van Cappellen, P. (2003). Predicting benthic fluxes of silicic acid from deep-sea
816 sediments. *J. Geophys. Res.: Oceans*, 108(C10).

817 Dixit, S., Van Cappellen, P., and Van Bennekom, A. J. (2001). Processes controlling solubility
818 of biogenic silica and pore water build-up of silicic acid in marine sediments. *Mar. Chem.*,
819 73:333–352.

820 Docquier, D., Fuentes-Franco, R., Koenigk, T., and Fichefet, T. (2020). Sea Ice—Ocean
821 Interactions in the Barents Sea Modeled at Different Resolutions. *Front. Earth Sci.*, 8(172).

822 Downes, P. P., Goult, S. J., Woodward, E. M. S., Widdicombe, C. E., Tait, K., and Dixon,
823 J. L. (2021). Phosphorus dynamics in the Barents Sea. *Limnol. Oceanogr.*, 66:S326–S342.

824 Dutkiewicz, A., Müller, R. D., O'Callaghan, S., and Jónasson, H. (2015). Census of seafloor
825 sediments in the world's ocean. *Geology*.

826 Egan, K. E., Rickaby, R. E., Leng, M. J., Hendry, K. R., Hermoso, M., Sloane, H. J., Bostock,
827 H., and Halliday, A. N. (2012). Diatom silicon isotopes as a proxy for silicic acid utilisation:
828 A Southern Ocean core top calibration. *Geochim. Cosmochim. Acta*, 96:174–192.

829 Ehlert, C., Doering, K., Wallmann, K., Scholz, F., Sommer, S., Grasse, P., Geilert, S., and
830 Frank, M. (2016a). Stable silicon isotope signatures of marine pore waters – Biogenic
831 opal dissolution versus authigenic clay mineral formation. *Geochim. Cosmochim. Acta*,
832 191:102–117.

Ehlert, C., Reckhardt, A., Greskowiak, J., Liguori, B. T., Böning, P., Paffrath, R., Brumsack, H. J., and Pahnke, K. (2016b). Transformation of silicon in a sandy beach ecosystem: Insights from stable silicon isotopes from fresh and saline groundwaters. *Chem. Geol.*, 440:207–218.

Fabre, S., Jeandel, C., Zambardi, T., Roustan, M., and Almar, R. (2019). An Overlooked Silica Source of the Modern Oceans: Are Sandy Beaches the Key? *Front. Earth Sci.*, 7.

Fahl, K., Stein, R., Gaye-Haake, B., Gebhardt, C., Kodina, L., Unger, D., and Ittekkot, V. (2003). Biomarkers in surface sediments from the Ob and Yenisei estuaries and the southern Kara Sea: Evidence for particulate organic carbon sources, pathways, and degradation. In Stein, R., Fahl, K., Fütterer, D., Galimov, E., and Stepanets, O., editors, *Siberian River Run-off in the Kara Sea: Characterisation, Quantification, Variability, and Environmental Significance*, pages 329–488. Elsevier, Amsterdam.

Fanning, K. A. and Schink, D. R. (1969). Interaction of Marine Sediments with Dissolved Silica. *Limnol. Oceanogr.*, 14(1):59–68.

Faust, J. C., Stevenson, M., Abbott, G., and Knies, J. (2020). Does Arctic warming reduce preservation of organic matter in Barents Sea sediments? *Philos. Trans. Royal Soc. A*, 378(2181).

Faust, J. C., Tessin, A., Fisher, B. J., Zindorf, M., Papadaki, S., Hendry, K. R., Doyle, K. A., and März, C. (2021). Millennial scale persistence of organic carbon bound to iron in Arctic marine sediments. *Nat. Commun.*, 12(275).

Fetterer, F., Savoie, M., Helfrich, S., and Clemente-Colón, P. (2010). *Multisensor Analyzed Sea Ice Extent - Northern Hemisphere (MASIE-NH), Version 1, Updated daily.* U.S. National Ice Center and National Snow and Ice Data Center, U.S.National Ice Center and National Snow and Ice Data Center (NSIDC), Boulder, Colorado USA.

Freitas, F. S., Hendry, K. R., Henley, S. F., Faust, J. C., Tessin, A. C., Stevenson, M. A.,

858 Abbott, G. D., März, C., and Arndt, S. (2020). Benthic-pelagic coupling in the Barents
859 Sea: an integrated data-model framework. *Philos. Trans. Royal Soc. A*, 378(20190359).

860 Frings, P. (2017). Revisiting the dissolution of biogenic Si in marine sediments: a key term
861 in the ocean Si budget. *Acta Geochim.*, 36:429–432.

862 Frings, P. J., Clymans, W., Fontorbe, G., De La Rocha, C. L., and Conley, D. J. (2016).
863 The continental Si cycle and its impact on the ocean Si isotope budget. *Chem. Geol.*,
864 425:12–36.

865 Gallinari, M., Ragueneau, O., Corrin, L., DeMaster, D. J., and Tréguer, P. (2002). The
866 importance of water column processes on the dissolution properties of biogenic silica in
867 deep-sea sediments I. Solubility. *Geochim. Cosmochim. Acta*, 66(15):2701–2717.

868 Geilert, S., Grasse, P., Doering, K., Wallmann, K., Ehlert, C., Scholz, F., Frank, M., Schmidt,
869 M., and Hensen, C. (2020). Impact of ambient conditions on the Si isotope fractionation
870 in marine pore fluids during early diagenesis. *Biogeosciences*, 17:1745–1763.

871 Georg, R. B., Reynolds, B. C., Frank, M., and Halliday, A. N. (2006). New sample prepara-
872 tion techniques for the determination of Si isotopic compositions using MC-ICPMS. *Chem.*
873 *Geol.*, 235(1-2):95–104.

874 Giesbrecht, K. E. (2019). *Biogenic Silica Dynamics of Arctic Marine Ecosystems*. PhD
875 thesis, University of Victoria.

876 Giesbrecht, K. E. and Varela, D. E. (2021). Summertime Biogenic Silica Production and
877 Silicon Limitation in the Pacific Arctic Region From 2006 to 2016. *Global Biogeochem.*
878 *Cycles*, 35.

879 Grasse, P., Brzezinski, M. A., Cardinal, D., De Souza, G. F., Andersson, P., Closset, I.,
880 Cao, Z., Dai, M., Ehlert, C., Estrade, N., François, R., Frank, M., Jiang, G., Jones,
881 J. L., Kooijman, E., Liu, Q., Lu, D., Pahnke, K., Ponzevera, E., Schmitt, M., Sun, X.,
882 Sutton, J. N., Thil, F., Weis, D., Wetzel, F., Zhang, A., Zhang, J., and Zhang, Z. (2017).

GEOTRACES inter-calibration of the stable silicon isotope composition of dissolved silicic acid in seawater. *J. Anal. At. Spectrom.*, 32(3):562–578.

Hammond, D. E., Cummins, K. M., Mcmanus, J., Berelson, W. M., Smith, G., and Spagnoli, F. (2004). Methods for measuring benthic nutrient flux on the California Margin: Comparing shipboard core incubations to in situ lander results. *Limnol. Oceanogr.: Methods*, 2(6):146–159.

Hátún, H., Azetsu-Scott, K., Somavilla, R., Rey, F., Johnson, C., Mathis, M., Mikolajewicz, U., Coupel, P., Tremblay, J., Hartman, S., Pacariz, S. V., Salter, I., and Ólafsson, J. (2017). The subpolar gyre regulates silicate concentrations in the North Atlantic. *Sci. Rep.*, 7(14576).

Haug, T., Bogstad, B., Chierici, M., Gjøsæter, H., Hallfredsson, E. H., Høines, Å. S., Hoel, A. H., Ingvaldsen, R. B., Jørgensen, L. L., Knutsen, T., Loeng, H., Naustvoll, L. J., Røttingen, I., and Sunnanå, K. (2017). Future harvest of living resources in the Arctic Ocean north of the Nordic and Barents Seas: A review of possibilities and constraints. *Fish. Res.*, 188:38–57.

Hawkings, J. R., Wadham, J. L., Benning, L. G., Hendry, K. R., Tranter, M., Tedstone, A., Nienow, P., and Raiswell, R. (2017). Ice sheets as a missing source of silica to the polar oceans. *Nat. Commun.*, 8(14198).

Hendry, K. R. and Andersen, M. B. (2013). The zinc isotopic composition of siliceous marine sponges: Investigating nature's sediment traps. *Chem. Geol.*, 354:33–41.

Hendry, K. R., Leng, M. J., Robinson, L. F., Sloane, H. J., Blusztjan, J., Rickaby, R. E., Georg, R. B., and Halliday, A. N. (2011). Silicon isotopes in Antarctic sponges: An interlaboratory comparison. *Antarct. Sci.*, 23:34–42.

Hendry, K. R. and Robinson, L. F. (2012). The relationship between silicon isotope fractionation in sponges and silicic acid concentration: Modern and core-top studies of biogenic opal. *Geochim. Cosmochim. Acta*, 81:1–12.

Holmes, R. M., McClelland, J. W., Peterson, B. J., Tank, S. E., Bulygina, E., Eglinton, T. I., Gordeev, V. V., Gurtovaya, T. Y., Raymond, P. A., Repeta, D. J., Staples, R., Striegl, R. G., Zhulidov, A. V., and Zimov, S. A. (2012). Seasonal and Annual Fluxes of Nutrients and Organic Matter from Large Rivers to the Arctic Ocean and Surrounding Seas. *Estuaries Coast*, 35(2):369–382.

Hopkins, J. (2018). The Changing Arctic Ocean Cruise JR16006, RRS James Clark Ross, Cruise Report No.51. Technical report.

Hughes, H. J., Delvigne, C., Korntheuer, M., De Jong, J., André, L., and Cardinal, D. (2011). Controlling the mass bias introduced by anionic and organic matrices in silicon isotopic measurements by MC-ICP-MS. *J. Anal. At. Spectrom.*, 26(9):1892–1896.

Hughes, H. J., Sondag, F., Santos, R. V., André, L., and Cardinal, D. (2013). The riverine silicon isotope composition of the Amazon Basin. *Geochim. Cosmochim. Acta*, 121:637–651.

Hurd, D. (1983). Physical and chemical properties of siliceous skeletons. In *Silicon Geochemistry and Biogeochemistry*, pages 187–244. Academic Press, London.

Hurd, D. C. (1973). Interactions of biogenic opal, sediment and seawater in the Central Equatorial Pacific. *Geochim. Cosmochim. Acta*, 37:2257–2282.

Jakobsson, M., Grantz, A., Kristoffersen, Y., and Macnab, R. (2003). Physiographic provinces of the Arctic Ocean seafloor. *Geol. Soc. Am. Bull.*, 115(12):1443–1455.

Jakobsson, M., Mayer, L., Coakley, B., Dowdeswell, J. A., Forbes, S., Fridman, B., Hodnesdal, H., Noormets, R., Pedersen, R., Rebesco, M., Schenke, H. W., Zarayskaya, Y., Accettella, D., Armstrong, A., Anderson, R. M., Bienhoff, P., Camerlenghi, A., Church, I., Edwards, M., Gardner, J. V., Hall, J. K., Hell, B., Hestvik, O., Kristoffersen, Y., Marcussen, C., Mohammad, R., Mosher, D., Nghiem, S. V., Pedrosa, M. T., Travaglini, P. G., and Weatherall, P. (2012). The International Bathymetric Chart of the Arctic Ocean (IBCAO) Version 3.0. *Geophys. Res. Lett.*, 39(12).

Jeandel, C., Peucker-Ehrenbrink, B., Jones, M. T., Pearce, C. R., Oelkers, E. H., Godderis, Y., Lacan, F., Aumont, O., and Arsouze, T. (2011). Ocean margins: The missing term in oceanic element budgets? *Eos*, 92(26):217–224.

Jones, M. T., Pearce, C. R., and Oelkers, E. H. (2012). An experimental study of the interaction of basaltic riverine particulate material and seawater. *Geochim. Cosmochim. Acta*, 77:108–120.

Kamatani, A. and Oku, O. (2000). Measuring biogenic silica in marine sediments. *Mar. Chem.*, 68(3):219–229.

Karl, D. M. and Tien, G. (1992). MAGIC: A sensitive and precise method for measuring dissolved phosphorus in aquatic environments. *Limnol. Oceanogr.*, 37(1):105–116.

Khalil, K., Rabouille, C., Gallinari, M., Soetaert, K., DeMaster, D. J., and Ragueneau, O. (2007). Constraining biogenic silica dissolution in marine sediments: A comparison between diagenetic models and experimental dissolution rates. *Mar. Chem.*, 106:223–238.

Kim, J., Dong, H., Seabaugh, J., Newell, S. W., and Eberl, D. D. (2004). Role of Microbes in the Smectite-to-Illite Reaction. *Science*, 303:830–832.

King, S., Froelich, P., and Jahnke, R. (2000). Early diagenesis of germanium in sediments of the Antarctic South Atlantic: In search of the missing Ge sink. *Geochim. Cosmochim. Acta*, 64(8):1375–1390.

Koning, E., Epping, E., and Van Raaphorst, W. (2002). Determining biogenic silica in marine samples by tracking silicate and aluminium concentrations in alkaline leaching solutions. *Aquat. Geochem.*, 8:37–67.

Krause, J. W., Duarte, C. M., Marquez, I. A., Assmy, P., Fernández-Méndez, M., Wiedmann, I., Wassmann, P., Kristiansen, S., and Agustí, S. (2018). Biogenic silica production and diatom dynamics in the Svalbard region during spring. *Biogeosciences*, 15(21):6503–6517.

Krause, J. W., Schulz, I. K., Rowe, K. A., Dobbins, W., Winding, M. H., Sejr, M. K., Duarte, C. M., and Agustí, S. (2019). Silicic acid limitation drives bloom termination and potential carbon sequestration in an Arctic bloom. *Sci. Rep.*, 9(8149).

Krissansen-Totton, J. and Catling, D. C. (2020). A coupled carbon-silicon cycle model over Earth history: Reverse weathering as a possible explanation of a warm mid-Proterozoic climate. *Earth Planet. Sci. Lett.*, 537(116181).

Kulikov, N. (2004). Amorphous silica contents in bottom sediments from the Kara Sea. *PANGAEA*.

Lalande, C., Bauerfeind, E., Nöthig, E. M., and Beszczynska-Möller, A. (2013). Impact of a warm anomaly on export fluxes of biogenic matter in the eastern Fram Strait. *Prog. Oceanogr.*, 109:70–77.

Lawson, D. S., Hurd, D. C., and Pankratz, H. S. (1978). Silica dissolution rates of decomposing phytoplankton assemblages at various temperatures. *Am. J. Sci.*, 278:1373–1393.

Lerman, A., Mackenzie, F. T., and Bricker, O. P. (1975). Rates of dissolution of aluminosilicates in seawater. *Earth Planet. Sci. Lett.*, 25(1):82–88.

Lien, V. S., Vikebø, F. B., and Skagseth, O. (2013). One mechanism contributing to covariability of the Atlantic inflow branches to the Arctic. *Nat. Commun.*, 4(1488).

Liguori, B. T., Ehlert, C., and Pahnke, K. (2020). The Influence of Water Mass Mixing and Particle Dissolution on the Silicon Cycle in the Central Arctic Ocean. *Front. Earth Sci.*, 7(202).

Lind, S., Ingvaldsen, R. B., and Furevik, T. (2018). Arctic warming hotspot in the northern Barents Sea linked to declining sea-ice import. *Nature Climate Change*, 8:634–639.

Loucaides, S., Koning, E., and Van Cappellen, P. (2012). Effect of pressure on silica solubility of diatom frustules in the oceans: Results from long-term laboratory and field incubations. *Mar. Chem.*, 136-137:1–6.

Loucaides, S., Michalopoulos, P., Presti, M., Koning, E., Behrends, T., and Van Cappellen, P. (2010). Seawater-mediated interactions between diatomaceous silica and terrigenous sediments: Results from long-term incubation experiments. *Chem. Geol.*, 270:68–79.

Mackenzie, F. and Garrels, R. (1965). Silicates: Reactivity with Sea Water. *Science*, 150(3692):57–58.

Mackenzie, F. T., Garrels, R. M., Bricker, O. P., and Bickley, F. (1967). Silica in sea water: Control by silica minerals. *Science*, 155(3768):1404–1405.

Maldonado, M., López-Acosta, M., Sitjà, C., García-Puig, M., Galobart, C., Ercilla, G., and Leynaert, A. (2019). Sponge skeletons as an important sink of silicon in the global oceans. *Nat. Geosci.*, 12:815–822.

Martin, W. and Bender, M. (1988). The variability of benthic fluxes and sedimentary remineralization rates in response to seasonally variable organic carbon rain rates in the deep sea; a modeling study. *Am. J. Sci.*, 288(6):561–574.

März, C., Meinhardt, A. K., Schnetger, B., and Brumsack, H. J. (2015). Silica diagenesis and benthic fluxes in the Arctic Ocean. *Mar. Chem.*, 171:1–9.

McManus, J., Hammond, D. E., Berelson, W. M., Kilgore, T. E., Demaster, D. J., Ragueneau, O. G., and Collier, R. W. (1995). Early diagenesis of biogenic opal: Dissolution rates, kinetics, and paleoceanographic implications. *Deep. Res. II*, 42(2-3):871–903.

Michalopoulos, P. and Aller, R. C. (1995). Rapid clay mineral formation in Amazon delta sediments: Reverse weathering and oceanic elemental cycles. *Science*, 270:614–617.

Michalopoulos, P. and Aller, R. C. (2004). Early diagenesis of biogenic silica in the Amazon delta: Alteration, authigenic clay formation, and storage. *Geochim. Cosmochim. Acta*, 68(5):1061–1085.

Middag, R., de Baar, H. J., Laan, P., and Bakker, K. (2009). Dissolved aluminium and the silicon cycle in the Arctic Ocean. *Mar. Chem.*, 115(3-4):176–195.

Mortlock, R. A. and Froelich, P. N. (1989). A simple method for the rapid determination of biogenic opal in pelagic marine sediments. *Deep. Res. A*, 36(9):1415–1426.

Neukermans, G., Oziel, L., and Babin, M. (2018). Increased intrusion of warming Atlantic water leads to rapid expansion of temperate phytoplankton in the Arctic. *Glob. Change Biol.*, 24(6):2545–2553.

Ng, H. C., Cassarino, L., Pickering, R. A., Woodward, E. M. S., Hammond, S. J., and Hendry, K. R. (2020). Sediment efflux of silicon on the Greenland margin and implications for the marine silicon cycle. *Earth Planet. Sci. Lett.*, 529(115877).

Odin, G. S. and Fröhlich, F. (1988). Chapter C3 Glaucony from the Kerguelen Plateau (Southern Indian Ocean). *Dev. Sedimentol.*, 45:277–294.

Olli, K., Wexels Riser, C., Wassmann, P., Ratkova, T., Arashkevich, E., and Pasternak, A. (2002). Seasonal variation in vertical flux of biogenic matter in the marginal ice zone and the central Barents Sea. *J. Mar. Syst.*, 38:189 – 204.

Opfergelt, S. and Delmelle, P. (2012). Silicon isotopes and continental weathering processes: Assessing controls on Si transfer to the ocean. *C. R. - Geosci.*, 344:723–738.

Orkney, A., Platt, T., Narayanaswamy, B. E., Kostakis, I., and Bouman, H. A. (2020). Bio-optical evidence for increasing Phaeocystis dominance in the Barents Sea: Increasing Phaeocystis in Barents Sea. *Philos. Trans. Royal Soc. A*, 378(2181).

Oziel, L., Neukermans, G., Ardyna, M., Lancelot, C., Tison, J. L., Wassmann, P., Sirven, J., Ruiz-Pino, D., and Gascard, J. C. (2017). Role for Atlantic inflows and sea ice loss on shifting phytoplankton blooms in the Barents Sea. *J. Geophys. Res.: Oceans*, 122(6):5121–5139.

Oziel, L., Sirven, J., and Gascard, J. C. (2016). The Barents Sea frontal zones and water masses variability (1980-2011). *Ocean Sci.*, 12:169–184.

Pickering, R., Cassarino, L., Hendry, K., Wang, X., Maiti, K., and Krause, J. (2020). Using Stable Isotopes to Disentangle Marine SedimentarySignals in Reactive Silicon Pools. *Geophys. Res. Lett.*, 47(15).

Pirrung, M., Illner, P., and Matthiessen, J. (2008). Biogenic barium in surface sediments of the European Nordic Seas. *Mar. Geol.*, 250(1-2):89–103.

Rabouille, C., Gaillard, J. F., Tréguer, P., and Vincendeau, M. A. (1997). Biogenic silica recycling in surficial sediments across the Polar Front of the Southern Ocean (Indian Sector). *Deep. Res. II*, 44(5):1151–1176.

Ragueneau, O., Gallinari, M., Corrin, L., Grandel, S., Hall, P., Hauvespre, A., Lampitt, R. S., Rickert, D., Stahl, H., Tengberg, A., and Witbaard, R. (2001). The benthic silica cycle in the Northeast Atlantic: Annual mass balance, seasonality, and importance of non-steady-state processes for the early diagenesis of biogenic opal in deep-sea sediments. *Prog. Oceanogr.*, 50(1-4):171–200.

Ragueneau, O., Savoye, N., Del Amo, Y., Cotten, J., Tardiveau, B., and Leynaert, A. (2005). A new method for the measurement of biogenic silica in suspended matter of coastal waters: Using Si:Al ratios to correct for the mineral interference. *Cont. Shelf Res.*, 25:5–6.

Ragueneau, O. and Tréguer, P. (1994). Determination of biogenic silica in coastal waters: applicability and limits of the alkaline digestion method. *Mar. Chem.*, 45(1-2):43–51.

Ragueneau, O., Tréguer, P., Leynaert, A., Anderson, R. F., Brzezinski, M. A., DeMaster, D. J., Dugdale, R. C., Dymond, J., Fischer, G., François, R., Heinze, C., Maier-Reimer, E., Martin-Jézéquel, V., Nelson, D. M., and Quéguiner, B. (2000). A review of the Si cycle in the modern ocean: Recent progress and missing gaps in the application of biogenic opal as a paleoproductivity proxy. *Glob. Planet. Change*, 26(4):317–365.

Rahman, S., Aller, R. C., and Cochran, J. K. (2016). Cosmogenic 32Si as a tracer of biogenic silica burial and diagenesis: Major deltaic sinks in the silica cycle. *Geophys. Res. Lett.*

Rahman, S., Aller, R. C., and Cochran, J. K. (2017). The Missing Silica Sink: Revisiting the Marine Sedimentary Si Cycle Using Cosmogenic 32Si. *Global Biogeochem. Cycles*, 31(10):1559–1578.

Rahn, K. A. (1976). Silicon and aluminum in atmospheric aerosols: Crust-air fractionation? *Atmos. Environ.*, 10:597–601.

Rebreanu, L., Vanderborght, J. P., and Chou, L. (2008). The diffusion coefficient of dissolved silica revisited. *Mar. Chem.*, 112:230–233.

Reigstad, M., Wassmann, P., Wexels Riser, C., Øygarden, S., and Rey, F. (2002). Variations in hydrography, nutrients and chlorophyll a in the marginal ice-zone and the central Barents Sea. *J. Mar. Syst.*, 38:9–29.

Ren, H., Brunelle, B. G., Sigman, D. M., and Robinson, R. S. (2013). Diagenetic aluminum uptake into diatom frustules and the preservation of diatom-bound organic nitrogen. *Mar. Chem.*, 155:92–101.

Rey, F. (2012). Declining silicate concentrations in the Norwegian and Barents Seas. *ICES J. Mar. Sci.*, 69(2):208–212.

Reynolds, B. C., Aggarwal, J., André, L., Baxter, D., Beucher, C., Brzezinski, M. A., Engström, E., Georg, R. B., Land, M., Leng, M. J., Opfergelt, S., Rodushkin, I., Sloane, H. J., Van Den Boorn, S. H., Vroon, P. Z., and Cardinal, D. (2007). An inter-laboratory comparison of Si isotope reference materials. *J. Anal. At. Spectrom.*, 22(5):561–568.

Rickert, D. (2000). Dissolution kinetics of biogenic silica in marine environments. *Ber. Zur Polarforschung*, 351.

Rickert, D., Schlüter, M., and Wallmann, K. (2002). Dissolution kinetics of biogenic silica from the water column to the sediments. *Geochim. Cosmochim. Acta*, 66(3):439–455.

Sakshaug, E. (1997). Biomass and productivity distributions and their variability in the Barents Sea. *ICES J. Mar. Sci.*, 54(3):341–350.

Sayles, F. L., Deuser, W. G., Goudreau, J. E., Dickinson, W. H., Jickells, T. D., and King, P. (1996). The benthic cycle of biogenic opal at the Bermuda Atlantic Time Series site. *Deep. Res. I*, 43(4):383–409.

Sayles, F. L., Martin, W. R., Chase, Z., and Anderson, R. F. (2001). Benthic remineralization and burial of biogenic SiO2, CaCO3, organic carbon, and detrital material in the Southern Ocean along a transect at 170° West. *Deep. Res. II*, 48(19-20):4323–4383.

Sayles, F. L., Martin, W. R., and Deuser, W. G. (1994). Response of benthic oxygen demand to particulate organic carbon supply in the deep sea near Bermuda. *Nature*, 371:686–689.

Schink, D. R., Guinasso, N. L., and Fanning, K. A. (1975). Processes affecting the concentration of silica at the sediment-water interface of the Atlantic Ocean. *J. Geophys. Res.*, 80(21):3013–3031.

Schlüter, M. and Sauter, E. (2000). Biogenic silica cycle in surface sediments of the Greenland Sea. *J. Mar. Syst.*, 23(4):333–342.

Siever, R. (1968). Establishment of equilibrium between clays and sea water. *Earth Planet. Sci. Lett.*, 5:106–110.

Smedsrud, L. H., Esau, I., Ingvaldsen, R. B., Eldevik, T., Haugan, P. M., Li, C., Lien, V. S., Olsen, A., Omar, A. M., Risebrobakken, B., Sandø, A. B., Semenov, V. A., and Sorokina, S. A. (2013). The role of the Barents Sea in the Arctic climate system. *Rev. Geophys.*, 51(3):415–449.

Solan, M. (2018). The Changing Arctic Ocean: Cruise Report, RRS James Clark Ross JR17007. Technical report.

Strickland, J. and Parsons, T. (1972). *A Practical Handbook of Seawater Analysis*, volume 167. Fisheries Research Board of Canada.

Sutton, J. N., André, L., Cardinal, D., Conley, D. J., De Souza, G. F., Dean, J., Dodd, J., Ehlert, C., Ellwood, M. J., Frings, P. J., Grasse, P., Hendry, K., Leng, M. J., Michalopou-

los, P., Panizzo, V. N., and Swann, G. E. (2018). A review of the stable isotope biogeochemistry of the global silicon cycle and its associated trace elements. *Front. Earth Sci.*, 5.

Sutton, J. N., Varela, D. E., Brzezinski, M. A., and Beucher, C. P. (2013). Species-dependent silicon isotope fractionation by marine diatoms. *Geochim. Cosmochim. Acta*, 104:300–309.

Tréguer, P., Nelson, D. M., Van Bennekom, A. J., Demaster, D. J., Leynaert, A., and Quéguiner, B. (1995). The silica balance in the world ocean: A reestimate. *Science*, 268:375–379.

Tréguer, P. J. and De La Rocha, C. L. (2013). The World Ocean Silica Cycle. *Ann. Rev. Marine Sci.*, 5:477–501.

Tréguer, P. J., Sutton, J. N., Brzezinski, M., Charette, M. A., Devries, T., Dutkiewicz, S., Ehlert, C., Hawkings, J., Leynaert, A., Liu, S. M., Monferrer, N. L., López-Acosta, M., Maldonado, M., Rahman, S., Ran, L., and Rouxel, O. (2021). Reviews and syntheses: The biogeochemical cycle of silicon in the modern ocean. *Biogeosciences*, 18:1269–1289.

van Bennekom, A. J., Fred Jansen, J. H., van der Gaast, S. J., van Iperen, J. M., and Pieters, J. (1989). Aluminium-rich opal: an intermediate in the preservation of biogenic silica in the Zaire (Congo) deep-sea fan. *Deep. Res. A*, 36(2):173–190.

Van Cappellen, P. and Qiu, L. (1997). Biogenic silica dissolution in sediments of the Southern Ocean. I. Solubility. *Deep. Res. II*, 44:1109–1128.

Van Den Boorn, S. H., Vroon, P. Z., and Van Bergen, M. J. (2009). Sulfur-induced offsets in MC-ICP-MS silicon-isotope measurements. *J. Anal. At. Spectrom.*, 24(8):1111–1114.

Varela, D. E., Brzezinski, M. A., Beucher, C. P., Jones, J. L., Giesbrecht, K. E., Lansard, B., and Mucci, A. (2016). Heavy silicon isotopic composition of silicic acid and biogenic silica in Arctic waters over the Beaufort shelf and the Canada Basin. *Global Biogeochem. Cycles*, 30(6):804–824.

Wassmann, P. and Olli, K. (2004). Central Barents Sea and Northern Spitsbergen. In *The Organic Carbon Cycle in the Arctic Ocean*, pages 112–114.

Wassmann, P., Ratkova, T., Andreassen, I., Vernet, M., Pedersen, G., and Rey, F. (1999). Spring bloom development in the marginal ice zone and the central Barents Sea. *Mar. Ecol.*, 20(3-4):321–346.

Wassmann, P., Reigstad, M., Haug, T., Rudels, B., Carroll, M. L., Hop, H., Gabrielsen, G. W., Falk-Petersen, S., Denisenko, S. G., Arashkevich, E., Slagstad, D., and Pavlova, O. (2006a). Food webs and carbon flux in the Barents Sea. *Prog. Oceanogr.*, 71(2-4):232–287.

Wassmann, P., Slagstad, D., Riser, C. W., and Reigstad, M. (2006b). Modelling the ecosystem dynamics of the Barents Sea including the marginal ice zone: II. Carbon flux and interannual variability. *J. Mar. Syst.*, 59(1-2):1–24.

Wetzel, F., de Souza, G. F., and Reynolds, B. C. (2014). What controls silicon isotope fractionation during dissolution of diatom opal? *Geochim. Cosmochim. Acta*, 131:128–137.

Willey, J. D. (1978). Release and uptake of dissolved silica in seawater by marine sediments. *Mar. Chem.*, 7:53–65.

Wollast, R. (1974). The Silica Problem. In Goldberg, E., editor, *The Sea, Volume 5: The Global Coastal Ocean*, chapter 11, pages 359–392. Harvard University Press.

Zheng, X. Y., Beard, B. L., Reddy, T. R., Roden, E. E., and Johnson, C. M. (2016). Abiologic silicon isotope fractionation between aqueous Si and Fe(III)-Si gel in simulated Archean seawater: Implications for Si isotope records in Precambrian sedimentary rocks. *Geochim. Cosmochim. Acta*, 187:102–122.

Figure 1: Map of ChAOS sampling stations and schematic of water mass circulation in the Barents Sea (PF- Polar Front (oceanic), AW- Atlantic Water, ArW- Arctic Water,

NCCW- Norwegian Coastal Current Water, BSW- Barents Sea Water, BSO- Barents Sea Opening, BSX- Barents Sea Exit. Dotted current paths represent subducted water masses (Lien et al., 2013)). The Barents Sea has a mean water depth of 230 m and is the largest of seven shelf seas encircling the Arctic Ocean, covering 1.4×10^6 km^2 (Sakshaug, 1997). NCCW and warm AW flow northwards through the BSO, while colder, relatively nutrient poor ArW flows southwards (Oziel et al., 2016; Årthun et al., 2012). The PF delineates the northern, ArW sector which is seasonally ice-covered (August-September minima, March-April maxima) and the AW dominated region to the south, which is kept perennially ice-free by the warmth of the AW. The bathymetry of the Barents Sea is characterised by the juxtaposition of deep troughs and shallow banks, which topographically constrain the PF in the western shelf, rendering it's position relatively stable (Oziel et al., 2016). This is in contrast to the eastern branch of the PF, which presents with significant positional variability on seasonal and interannual timescales (Smedsrud et al., 2013). The mixing of water masses, coupled with brine rejection from sea ice formation on the shallow banks forms denser BSW, which cascades to greater depths in a northeasterly direction, draining into the Arctic Ocean through the BSX (Smedsrud et al., 2013). BSW is thought to be critical for ventilation of the deep Arctic Ocean and for regional atmospheric CO_2 sequestration (Oziel et al., 2016; Smedsrud et al., 2013). Bathymetry data is from the GEBCO 2014 dataset (Jakobsson et al., 2012).

Figure 2: Compilation of all [DSi] depth profiles analysed on board the three ChAOS cruises. Top row: southern, Atlantic water stations (B03, B13, B14 (PF)). Bottom row: northern, Arctic water stations (B15, B16, B17). Includes all three Multicorer deployments per station for each cruise year.

Figure 3: B13, B14 and B15 pore water $\delta^{30}Si_{DSi-PW}$ and [DSi] depth profiles for the three ChAOS cruises, as well as pore water [Fe] (open symbols) (Faust et al., 2021) and depletion in NO_3^- (closed symbols) relative to core top water concentrations from 2017 (Freitas

et al., 2020). Top row: B13 (black) and B15 (grey), bottom row: B14. Error bars represent $\pm 2\sigma$ of the long term reproducibility of Diatomite standard, unless the same value for measurement replicates was greater. Vertical dashed lines show the core top water composition ($\delta^{30}Si_{DSi-CT}$) for the three stations from 2017.

Figure 4: On-board core incubation experiment from 2019 (JR18006). Sampling carried out every 3 hours over a 24 hour period. Top row: Core top water [DSi] against the ratio of sampling time (hours) to core top height (cm). Gradient ('m') of the linear regressions represent the magnitude of the DSi benthic flux (mmol m^{-2} day^{-1}, where μM is equivalent to mmol m^{-3}). Gradient uncertainty is represented by 95% confidence limits, dashed lines depict 95% prediction bands. Bottom row: Si isotopic composition of the core top water ($\delta^{30}Si_{DSi-Inc}$). Error bars represent long term reproducibility of Si standards (2σ ± 0.14), unless 2σ of measurement replicates was greater.

Figure 5: A) BSi wt% for B13, B14 and B15 samples from the 2019 cruise. Error bars denote $\pm 2\sigma$ of sample triplicates. B) δ^{30}Si compilation from this study, includes all pore water and solid phase leachate measurements. $\delta^{30}Si_{NaOH}$ and $\delta^{30}Si_{HCl}$ values are grouped for the three stations (B13, B14, B15), as these values were indistinguishable within long term reproducibility.

Figure 6: A) Pore water $\delta^{30}Si_{DSi-PW}$ plotted against the inverse of the concentration (1/[DSi]). Mixing line was calculated following equation 7, from Geilert et al. (2020). Composition of BSi solution for each station is equivalent to $\delta^{30}Si_{Alk}$. B) Simulating Rayleigh fractionation during the uptake of DSi by diatoms from seawater (De La Rocha et al., 1997). Lines depict changes in δ^{30}Si of the DSi pool (blue) and the compositions of the instantaneously formed BSi (black) and accumulated BSi (red). Fractionation factors (ϵ) of -1.18‰ and -2.0‰ were used to calculate the compositions for the solid and dashed coloured lines respectively.

Figure 7: Comparison of sea ice conditions on the day of sampling at B14 (30th July 2017, 25th July 2018, 13th July 2019) compared to the sea ice extent on the 1st May of each cruise to demonstrate the disparity in ice melt across the three years. Left to right: JR16006 (summer 2017), JR17007 (2018), JR18006 (2019). Daily sea ice extent data from U.S. National Ice Center and National Snow and Ice Data Center (NSIDC) (Fetterer et al., 2010).

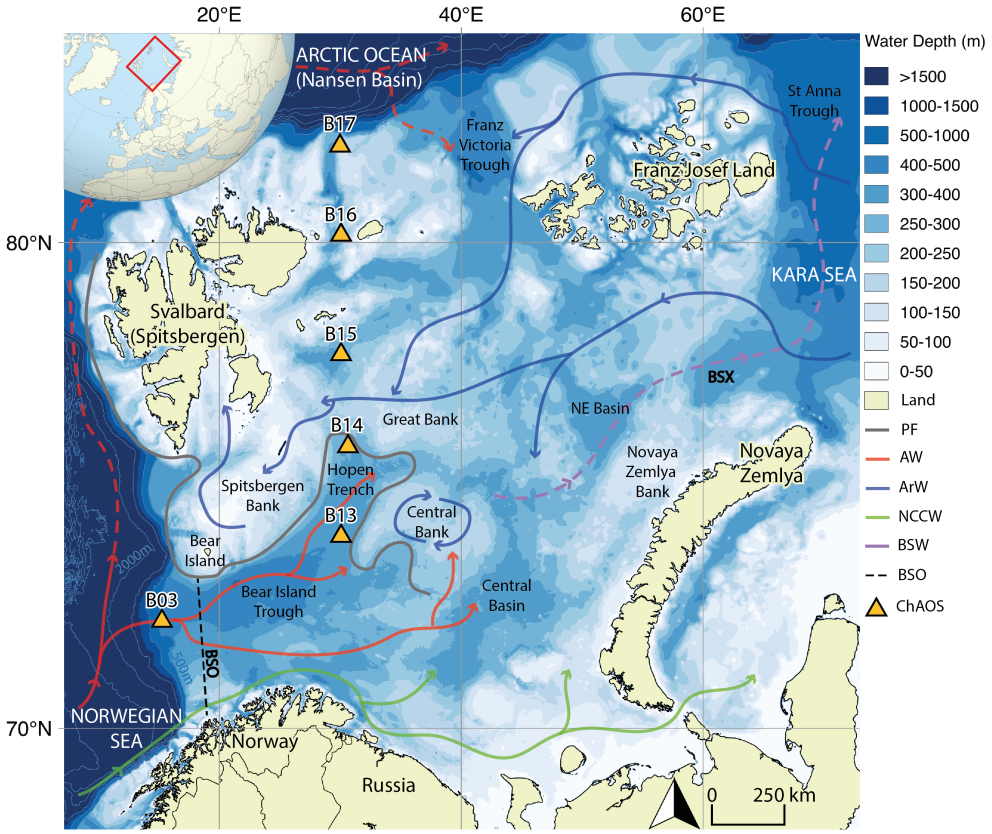

Figure 1:

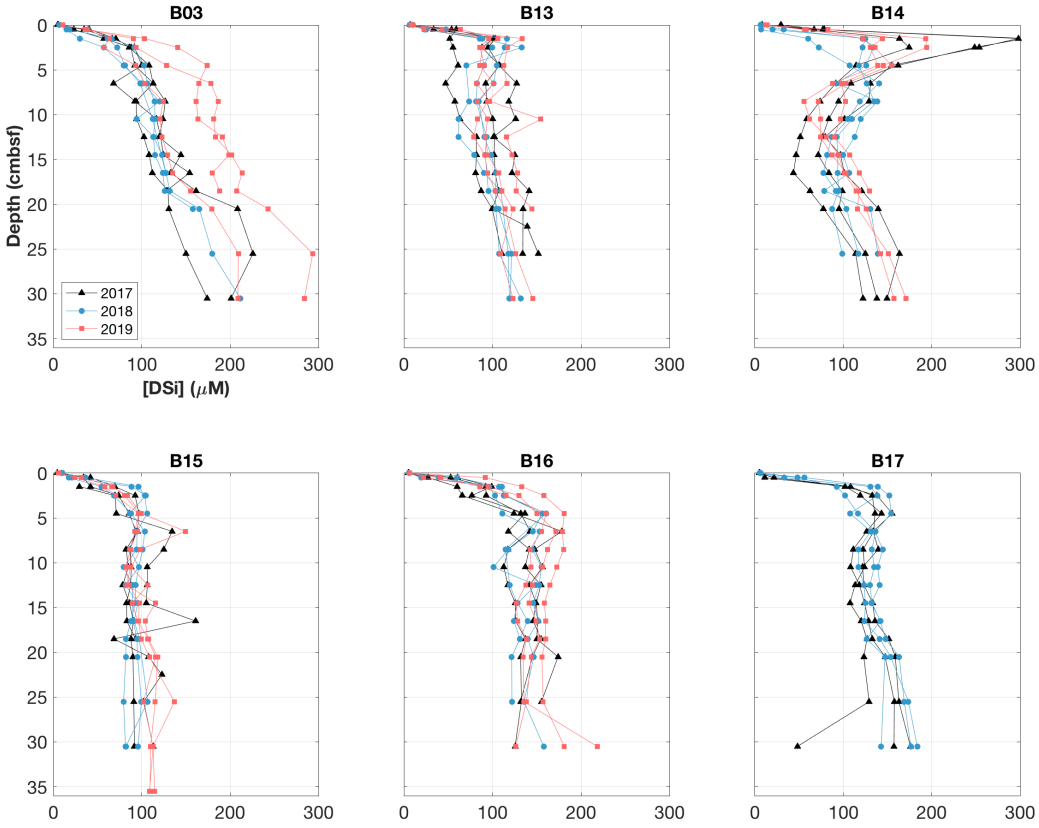
B03
B13
B14
B15
B16
B17
Depth (cmbsf)
[DSi] (μM)
2017
2018
2019
0
5
10
15
20
25
30
35
100
200
300

Figure 2:

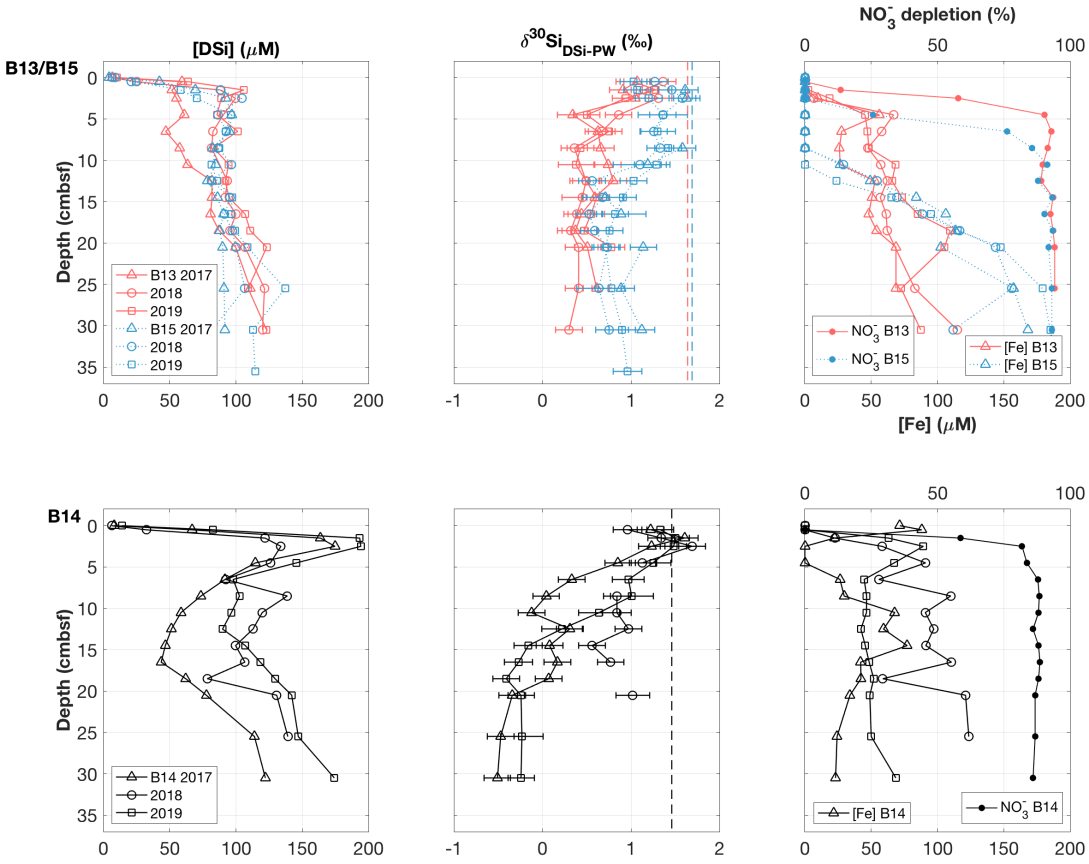
B13/B15
[DSi] (μM)
δ30SiDSi-PW (‰)
NO3- depletion (%)
Depth (cmbsf)
B13 2017
2018
2019
B15 2017
2018
2019
NO3- B13
NO3- B15
[Fe] B13
[Fe] B15
[Fe] (μM)
B14
B14 2017
2018
2019
[Fe] B14
NO3- B14

Figure 3:

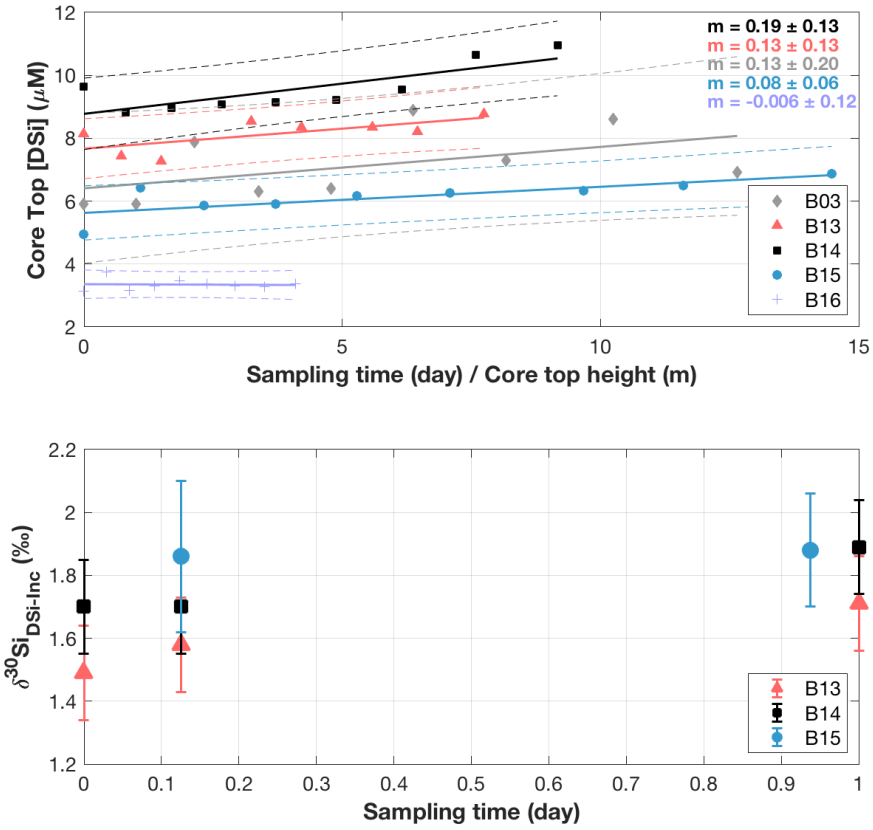
m = 0.19 ± 0.13
m = 0.13 ± 0.13
m = 0.13 ± 0.20
m = 0.08 ± 0.06
m = -0.006 ± 0.12
B03
B13
B14
B15
B16
Core Top [DSi] (μM)
Sampling time (day) / Core top height (m)
δ30SiDSi-Inc (‰)
Sampling time (day)

Figure 4:

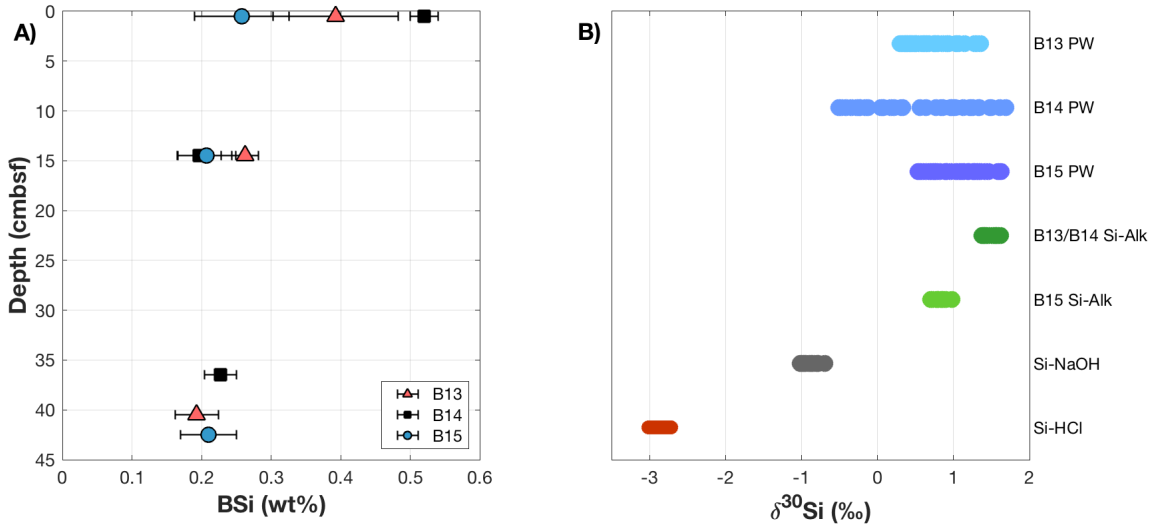

Figure 5:

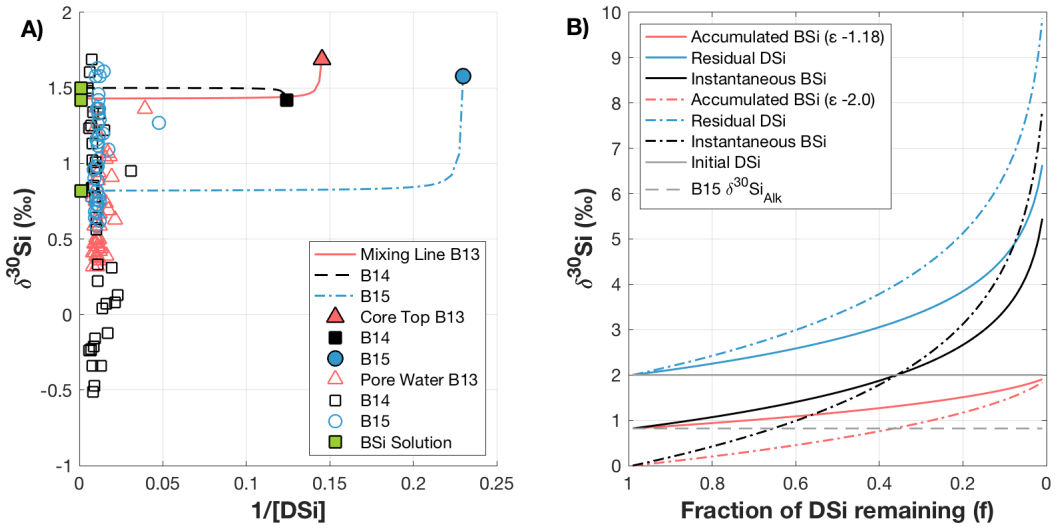

Figure 6:

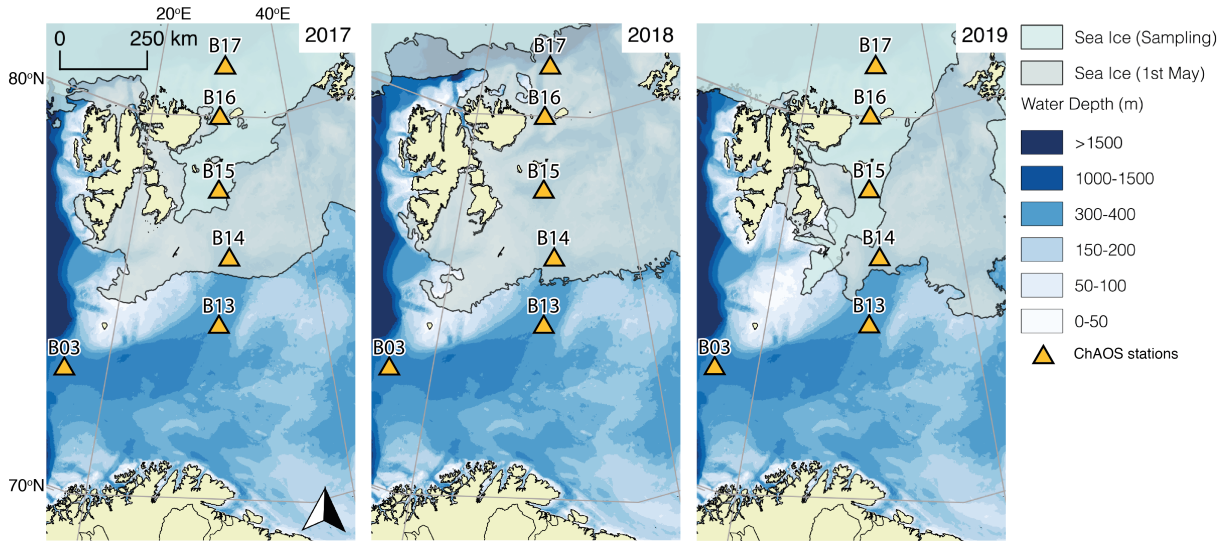
20°E
40°E
0
250 km
2017
2018
2019
80°N
70°N
B17
B16
B15
B14
B13
B03
Sea Ice (Sampling)
Sea Ice (1st May)
Water Depth (m)
>1500
1000-1500
300-400
150-200
50-100
0-50
ChAOS stations

Figure 7: